

## Author Response

We are grateful for the detailed review from Dr. Mike Fromm and believe that the manuscript has been significantly improved in addressing his concerns. The following response is formatted as follows: (1) Overview of changes, (2) detailed responses, and (3) the revised manuscript showing tracked-changes.

### **1. Overview of Changes:**

The reviewer requested substantial improvements to the manuscript in three main categories:

- (1) A more thorough explanation of the data processing methods
- (2) Improved clarity in the lidar data visualization
- (3) Fuller use of strategic ancillary data such as radar and surface weather data.

We have addressed each of these issues as follows:

1. A Data and Methods section was added describing:
  - a. The lidar observing systems.
  - b. Lidar-smoke interactions.
  - c. Lidar scan strategies
  - d. Lidar data post processing and edge detection algorithm (see below).
  - e. Velocity-Azimuth Display (VAD) wind profile retrieval.
  - f. Radar sources and data analysis
  - g. Satellite data
  - h. Radiosonde data and parcel analysis
2. All of the lidar data have been re-plotted using a pixel-colored mesh instead of scattered circles. Included in these figures are the plume edge detection and beam attenuation points. Additional efforts have been made throughout to make the visualizations easier to interpret.
3. We have significantly added the use of ancillary data including:
  - a. Radar derived 3D renderings of the pyroCu/Cb (**Figs. 7c, 16c**)
  - b. Time series of radar echo tops (**Figs. 7b, 16b**)
  - c. Dual polarization differential reflectivity data for the Bald Fire case (**Fig. 8**).
  - d. Additional satellite observations from GOES and MODIS (**Figs. 4,11**)
  - e. Surface weather data for the Rocky Fire case (**Fig. 19**).

In addition, based on a number of the reviewer's questions we have introduced an improved plume edge and attenuation algorithm. Using this approach we present an analysis of the change in beam attenuation depth with height in the plume, which is indicative of the condensation level and corroborates the original suite of analyses inspecting the lidar backscatter alone. The algorithm is described and demonstrated in the Data and Methods section (**Section 2.1.3. Lines 149-172, Fig. 2**). The resulting edge detections and attenuation points are now included in the lidar plume rise examples in **Figs. 5, 12, and 13** and summary statistics for attenuation

## Author Response

depth are presented in **Figs. 6c and 15c**. These data show that attenuation of the lidar beam becomes much more rapid at the condensation level.

### **2. Detailed Responses:**

Below are detailed responses to the reviewers concerns. This section is formatted as follows: Reviewer comments in italics, responses in normal font, line and figure numbers of modifications in bold.

*Data and Methods: The two case studies are of course different, but they are approached with a similar measurement strategy and instrument suite. To the extent of the similarity, I think a separate section entitled "Data and Method" is called for. In this section LC can describe the Doppler lidar characteristics, derived products, ancillary data characteristics, the measurement strategy and chronology. E.g. when was measurement started w.r.t. pyroCu onset, how frequent were the scans? Were there any interruptions during the measurement interval?*

We have added an extensive data and methods section (**lines 93-222**). This section addresses the lidar characteristics, lidar-smoke interaction, lidar data post-processing, wind profile retrievals, radar data and interpretation, satellite data, radiosonde data, and more. The lidar post-processing to determine plume edges is also illustrated with a new figure (**Fig. 2**), which shows how the lidar signal-to-noise ratio (SNR) is used to isolate the plume.

We have also added an introductory map figure (**Fig. 1**), which orients the reader to the locations of the fires and observing systems. Additional map figures (**Figs. 3 and 9**) are included in the case studies of each fire to provide further details on the scan paths of the lidar and information about the fire growth patterns.

*Regarding all the lidar range-height type backscatter plots, the reader needs some basic information and a fuller description of the way the data are plotted:*

*\* There is a smooth gray background inside the measurement arc. But that shading appears to change with distance from the lidar. What is the reason for that?*

*\* Do the circles faithfully characterize the lidar spatial resolution?*

*\* There seems to be overlap of the circles in some locations. Does this represent multiple/overlapped samples of a given volume?*

*\* What range of azimuth is scanned?*

*\* How many scans comprise these views?*

*\* How much time is taken to fill the scans as shown?*

*\* The circles appear to be open; i.e. only the perimeter of the circle is shaded according to backscatter. Is that correct?*

*\* Some areas of these plots have a diffuse appearance (like the smoke above the lidar in the second case). Is this just a dense bunch of circles with near-homogeneous backscatter? Or is something else being plotted?*

Because of the significant questions about these plots, we have replotted all of the lidar data using a pixel-color mesh. In these figures the pixel size is the range gate length (18 m) and arc length between lidar beams (.7 deg for Bald Fire, 1 deg for the Rocky Fire). Whereas the earlier figures represented aggregated data from one or more RHIs (hence overlapping dots), the new figures each represent a single RHI

## Author Response

sweep. In addition, the range of azimuths scanned, the amount of time between scans, and the total scan duration are described in the text. Some of this information is in the methods (**Section 2.1.2 Lidar Scan Strategies**), some in the case study descriptions (**lines 248-254, lines 564-569, 582-583**).

We have also changed the way we present the attenuation of the lidar beam, as described and demonstrated in the methods section (**Section 2.1.3: Plume Edge Detection**). The leading plume edges are now shown in each figure as red dots and the attenuation point as blue dots. All data beyond the attenuation point are removed from the figures. Earlier figures used different attenuation criteria.

*Suggestion: Because of the lidar attenuation issue and because LC do employ NEXRAD data to some extent (echo top analysis), could the radar reflectivity data be gainfully employed along with the lidar data to characterize the pyrocloud in the lidar attenuation shadow? Would this add important information that strengthens the lidar analysis?*

This is was a great suggestion. The radar analysis in each case study has been significantly expanded in order to examine the pyroCu structure within the lidar attenuation shadow. Specifically, we have included 3D volume renderings of reflectivity data contemporaneous with the lidar scans (**Fig. 7c, Fig. 16c**) and time-series of the echo tops (**Fig. 7b, Fig 16b**). Discussion of the key features of these analyses is now included in the manuscript (**lines 319-339, 499-514**). In addition we include simple analysis of differential reflectivity data for the Bald Fire case (**Fig. 8, lines 340-350**) which shows the way in which the shape of radar targets change with height in the plume.

*P29051, L19. Smoke-particle size distributions usually show a mode between 100-200 nm. This does not seem to fall into the category of "micron-sized aerosol." I suggest fuller characterization of the lidar's wavelength and the range of particle sizes to which the lidar is sensitive.*

*In my viewing of the lidar range-height type plots, the distance from front-edge backscatter to total attenuation is as important to understand as the backscatter itself. I.e. the "shadow" behind the cloud is as indicative as the backscatter along the edge. This shadow is seen above/behind the cloud and at altitudes below the cloud as well. Hence there is some ambiguity as to what particles are causing the strong backscatter and shadowing in the different parts of the scanning column. This should be addressed. The Conclusions section mentions debris in the plume. I suspect that this might be a large factor in the strong attenuation below the presumed cloud base. I suggest that the authors discuss in detail the factors causing attenuation variations within and outside the cloud.*

These are all good points. A discussion of the lidar wavelength, smoke size distribution, and expected lidar-smoke scattering is now included in **Section 2.1.1: Lidar Sensitivity, lines 103-130**. The key point of this discussion is that the lidar's attenuated backscatter is likely to contain roughly equal contributions from the modal sub-micron particles and the sparser coarse particles. We also discuss the presence of super-giant aerosol and debris in the base of the plume and lidar-cloud interactions. The role of debris in attenuating the lidar beam is discussed. A number of new references have been added in support of this section.

*P29057 (Section 3.1): Winds displayed in Figure 8 are characterized "ambient" and reported in terms of compass direction and speed. Presumably these data are derived from the lidar. How are wind direction and speed calculated from the lidar data? The Doppler lidar is known to get radial wind information, but*

## Author Response

*it's not clear how 360-degree wind information is retrievable. Also, no information was given as to where the wind information comes from within the scanning volume of the lidar. Please elucidate.*

These winds are retrieved using the Velocity-Azimuth-Display (VAD) technique commonly used by lidars and radars to extract the horizontal wind from conical scan of the Doppler velocity (**Browning and Wexler 1968**). The technique uses a harmonic analysis of the radial velocity at each height. The zeroth harmonic provides the divergence of the wind, while the amplitude and phase of the 1<sup>st</sup> harmonic provide the wind speed and direction. We have added a short description of this in the methods sections, including the azimuth and elevation sweep angles used during the VADs (**lines 139-147**). The elevation angle for the conical scans was 50 degrees and the azimuths span 360 degrees. The scans take about 1 minute to complete.

*Section 3.1 Plume geometry being introduced here (P29057, L23-26), so some definition of "plume center" is called for. And the reader needs to know what the "objective" and "semi" parts are of the "semi-objective" delineation of plume "center." I bring this up because of the attenuation factor...there's presumably a lot of plume down-range of the wall of strong backscatter seen on the plots. That wall might rightly be viewed as the upwind edge of the updraft column, with an absence of knowledge of the true plume horizontal thickness and vertical shape. This part of the paper is intended to infer updraft velocity, which would be important to know. But to make this convincing, much more detail and clarity are needed.*

This section has been modified in light of your concerns about attenuation and the unknown depth of the plume (**Lines 463-480**). We now present just the first and last RHI scans from this pyroCu pulse and eliminate the plume centerline analysis. In addition we no longer attempt to extrapolate the updraft speed, and instead state:

**“The actual updraft speed likely exceeds these values since the radial velocity data only reflect the projection of the updraft onto the oblique lidar beam.”**

To discuss changes in the updraft we add a comparative histogram of the radial velocity data within the plume between the first and last time steps (**Fig 14c**). These data show a clear reduction in outbound radial velocity strength with time, and thus a reduction of the updraft. We also change the discussion of plume tilt to be more qualitative, asserting that the plume updraft becomes more sheared with time. This is further supported later in the manuscript by including the balloon ascent track, which shows the effect of the ambient shear on the ascent of a buoyant parcel (**Fig. 17b**)

*P29058, L4-8. Discussion of a smoke feature between the lidar and the pyrocloud: The sign-change boundary is inconsistent with the backscatter feature that extends from overhead to the pyroCu column. The zero line is 2300 m; winds below are away from the lidar yet the backscattering feature that is over the lidar bottoms out a few hundred meters lower. Moreover, this feature is over the lidar from the earliest time shown, which means if it came from the Rocky fire it was injected well before that time, and there is no wind data prior to that figure panel to determine where that might have come from. If that overhead smoke layer is to be discussed, I think another explanation, or a more rigorous defense of the present interpretation, is needed.*

## Author Response

We have significantly modified this section of the text and no longer discuss the lateral smoke layer in the context of the shear layer and plume interaction. For the sake of clarity, however, I have added smoke contours to the radial velocity figure (**Fig. 14c,d**) so that the reader may more easily see how the features correspond. As it were, the lateral smoke layer is centered on the shear layer, which is also a stable layer (see the sounding). Smoke without sufficient positive buoyancy to ascend out of the boundary layer becomes trapped at *the base* of this layer and spreads laterally. In addition some smoke from plume penetrating this layer would also be expected to detrain *within* this layer (e.g., the edges of the updraft are not buoyant enough to make it all the way through the inversion). We do not believe these particular points are important in the current analysis so we have not included them.

*Section 3.4, discussion of the two-day disparity in pyroconvection occurrence: This argument is interesting but may not tell the whole story. Does the MesoWest data include temperature and windspeed? Might there be a day-day difference in the windspeed near the fire that could explain the different fire behavior? By arguing that increased low-level moisture is partly responsible for the pyroCu, you're seemingly proposing a departure of the moisture component in the "hot, dry, windy" prescription for intense fire behavior. So I think it is important to look at wind, T, and RH in addition to absolute moisture.*

We have added additional meteorological analysis in **Fig 19** and in the discussion on **lines 561-583**. The weather data show that the “hot” and “windy” aspects of fire behavior do not vary significantly between days. Rather it is both the low level moisture (surface mixing ratio, and RH) and mid-level relative humidity that generate an environment where moist convection can occur and survive, albeit for a short time. For this, and many other reasons, I take issue with the “hot, dry, and windy” prescription for intense fire behavior but believe a thorough analysis of that argument is beyond the scope of this study.

*Figure 4 and 10: Please describe the fire-perimeter data. Is it from GOES? Fig. 1 has fire-perimeters but these are from MODIS, which are not at 00 UTC (local evening). So it seems these are from another source. The dotted and solid boundaries are not easy to discern due to overlap or proximity. I don't think there is discussion of the fire movement in the text, so do you need to make this distinction? Are the methods consistent between Fig. 4 and 10?*

The fire perimeter data are from the US Forest Service National Infrared Operations (NIROPS) flights conducted on large wildfire incidents (<http://nirops.fs.fed.us/>). This has been clarified in the text and in the figure captions. We have also changed the plotting in each figure to make it easier to distinguish between the perimeters on each day. We have also added a discussion of the fire growth, including the area burned to each case study (**lines 233-240, 562-565**).). To the best of our knowledge the methods for producing these perimeters are consistent with one another.

*Figure 12: Is it possible that the time here is UTC, not PDT? According to the figure the FRP peaks at 11pm-12 am local time on these two days. This is inconsistent with my expectations; which would have fire intensity peaking closer to late afternoon.*

## Author Response

The times are in PDT, as displayed, and the FRP does in fact peak near local midnight. I have added the MODIS-terra and Aqua FRP to **Fig. 19a** to corroborate the diurnal pattern. This would be an interesting topic for further investigation, namely nocturnal fire behavior, but is beyond the scope of this study (which has already lengthened appreciably). One factor that very likely contributed to the delayed onset of fire growth is *smoke shading* (Robock 1991; Lareau and Clements 2015). Lingering smoke in the boundary layer from the first day's fire growth and continued smoldering lead to reduced solar radiation throughout the morning. Only once the CBL developed sufficiently in the late afternoon did fire behavior pick up and deep plumes begin to form. Why the fire activity continues at night is an open question.

*P29051, discussion of Fig. 1: Is it worth it to give the Terra FRP too, in order to partially characterize the fire intensification from morning to afternoon?*

The MODIS-Terra FRP data at 1245 PDT have been included in the text (**lines 239-244**). This section now reads:

“The total FRP from the Bald Fire at the time of the MODIS-Aqua image was 19700 MW summed over 30 fire pixels. The pixel maximum was 2258 MW, though the pyroCu obscures a substantial portion of the fire. For comparison, the earlier MODIS-Terra overpass at 1245 PDT yielded a maximum FRP of just 829 MW and a total FRP of 3836 MW summed over 13 fire pixels. Clearly the fire experienced rapid change in size and intensity during the early afternoon, coincident with the development of the pyroCu.”

*P29051, L19: Inform the reader of the lidar's wavelength.*

An extensive discussion of lidar wavelength and scattering interactions has been included. (**lines 103-130**).

*P29051, L21-23: Can you give a number for the smoke SNR? Isn't this issue part and parcel of the above question about the lidar wavelength and particle sensitivity?*

A discussion of the lidar SNR and its use in the plume detection algorithm are included on **Lines 148-171**. A threshold SNR+1 of 1.01 is used, though changing the threshold is of relatively minor consequence and does not affect interpretation of the results. We have also included a new figure, **Fig. 2**, which shows the SNR data for a beam intersecting the base of the smoke plume and a beam interacting with cloud water.

*P29052, L11-15, discussion of plume geometry and vortices: Isn't the feature being described here just a signature of the cellular nature of cumulus, i.e. the cauliflower texture? Can one infer vortical circulations from these cloud-edge structures? It wasn't convincing to me, but perhaps this just needs to be explained in greater detail or supported with citations of previous such findings*

## Author Response

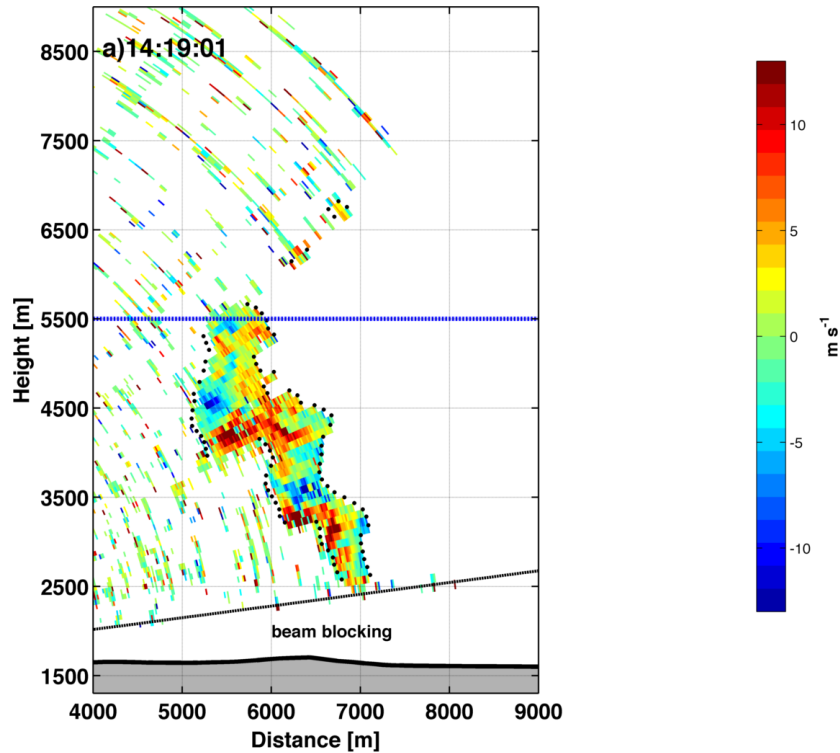


Figure R1. Radial velocity data showing vortical structures during the Bald Fire plume rise at 1419 PDT . Black dots indicate plume edge detections.

The circulations are clear when viewing the radial velocity data for the bald fire plume, which I have included here (Fig R1). These velocity data correspond to the backscatter data in **Fig. 5a** in the manuscript. The “stair-step” pattern along the leading plume edge corresponds to alternating regions of inbound and outbound velocities (warm vs. cool shading). These velocity couplets are clear signatures of vorticity along the plume edge.

The classic literature on thermals and plumes include discussions of the entrainment in these types of circulations (Scorer 1957, Woodward et al. 1959). Similar dynamics do exist in cumulus, though evaporation and sublimation of cloud water and ice are also part of that processes, whereas here we are looking at just the shear-induced vorticity along the edge of the updraft. In the interest of keeping the number of figures manageable I would prefer to not include additional velocity analyses for the Bald Fire. We do, however, have another manuscript in preparation from a different fire (The El Portal Fire) in which we explicitly examine plume vorticity and kinematic structure.

I have added the following text:

**Large coherent vortices are also apparent along the plume edge, especially in Fig. 5a,b as the “stair step” pattern in the plume edge detections. Based on the radial velocity data (not shown) the inward clefts in the plume edge correspond to enhanced flow into the plume (e.g., entrainment) and outward lobes reflecting flow**

## Author Response

**towards the lidar. Vortices of this sort are a well-known feature of rising thermals and plumes and play a leading role in entrainment (Scorer 1957; Woodward 1959).**

*Fire-generated debris is mentioned but only in the concluding section. If this is part of the signature seen in the lidar (and I believe it is), this should be discussed in the body of the paper too.*

Fire-generated debris is now discussed in the data and methods section, as is its expected role in attenuation. **Lines 115-125.**

*P29056. Section 3. Please inform the reader of the truck location and distance from the fire.*

The truck location and distances to the fires have been shown more clearly in **Figs. 1, 3, 4 and 10** and are now described in the text. The truck was ~7 km from the flanks of the Bald Fire and was within an already burned region of the Rocky Fire. The distance to the Rocky fire plumes varied between 2.5 and 7 km.

*P29056, L13-16: Were any measurements taken before the cloud formed? If so, what do they look like?*

There were measurements prior to the pyroCu observations, but these were mobile observations of dense smoke trapped near the surface. Figure R2 displays these backscatter data as a function of time and height above ground, where the ground height varies with time along the driving route. I have not geo-located these data to show the true height. The data show increasing smoke concentration within the boundary layer along the approach to the observing location that was used to document the PyroCu. There are also smoke small plumes in the boundary layer from smoldering portions of the fire that we drove past (e.g. just after 15:15 PDT). The next measurements after these were of the PyroCu data during the first flare-up of the Rocky Fire that afternoon (**Fig. 12**).

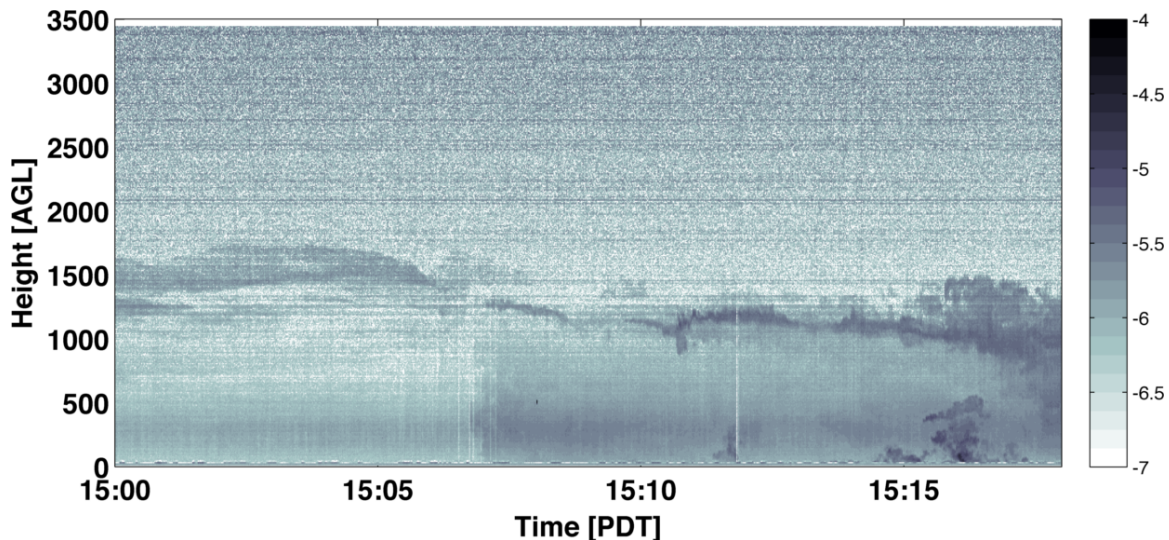


**Figure R2. Mobile lidar backscatter data from the approach to the observing location used to conduct RHI plume scans. PyroCu were not present at this time.**

## Author Response

*P29057, L3-5, discussion of second flare-up of Rocky fire: Was the lidar moved between these events? Fig 6 and 7 show that the fire plume is 1500-2000 m farther downrange during the 1800 event. If the lidar was not moved, does this signify that much of an advance of the fire front?*

The lidar location was not moved, but it was aimed along a different azimuth. The second flare up was from the eastern flank of the fire whereas the first flare up was on the NW flank. As such the change in range between these observations does not reflect an evolution in the fire front other than the eastern flank became the most active flank in the late afternoon. We have included a new figures for the Rocky Fire section, **Fig. 10**, which show the fire perimeters and lidar scan paths to make this more clear.

*P29057, L18-20: If the lidar wind info is coming predominantly from the upwind edge of the plume, the lowest returns are ~600 m above ground level. Hence I would contend that "near the surface" does not apply as well as, perhaps, "lowest-retrieved wind (roughly ??? m AGL)."*

These wind data are actually from a conical VAD scan above the lidar location, and the lowest data are about 50 m AGL. Hence we feel comfortable using “near surface” to describe the lowest portion of the wind profile.

*P29057, L27: It's not self evident how this number (18m/s) is arrived at. Please elaborate.*

We have removed this analysis and now simply state that the updraft likely exceeds the measured radial velocity.

*P29060, L19 (and generally throughout the paper): Either settle on a single time convention or give PDT as well as UTC here.*

All times are now in PDT.

*Figures 2, 6, 7: Suggestion: If all the photos were taken at the same location, the distance to the fire is constant among photos. Hence if they were all cropped at the same bottom geolocation, the analyst/reader could better compare the column vertical development.*

The photos were not all take at the exact same location making this suggestion difficult to implement. Since we believe the photos still provide the reader with a better sense of what the lidar is seeing we have opted to leave them as is.

*Figure 6, 7: It would be preferable for the RHI plots to have the same aspect ratio. They both go to 8000 m in the vertical but Fig 6 panels are squashed relative to Fig. 7.*

The aspect ratio is equal on all the RHI plots (meaning the x spacing is the same as the z spacing). In addition I have adjusted the range of the Rocky Fire figures to all be 0-6000 m in distance and 0-8000 m in height.

*Figure 7: What are the whitish blobs apparently lower than the cloud base in the 3 rightmost photos? Is this whiter smoke, or is it cloud? If it is an optical illusion of cloud, some explanation of what the eye beholds is called for.*

## Author Response

We believe, based on the literature and experience, that the “whitish blobs” are due to a change in the completeness of combustion favoring more hydrocarbon (organic carbon aerosol) in the plume. In contrast, earlier the combustion was less-complete flaming combustion, which produces more black carbon. I have added the following description in the text at **lines 610-617**:

**The photographs detailing the plume rise show changes in smoke color near the base of the convective column (Fig. 13a-d). For example, at 1805 PDT the smoke is a dark gray (Fig. 13a), whereas later the smoke is increasingly white (Fig. 13d). We believe the change in smoke coloration is associated with changes in the completeness of combustion: flaming combustion produces smoke dominated by black carbon aerosols, whereas smoldering combustion generates more organic carbon aerosol, which more effectively backscatter sunlight and appear whiter (Bellouin 2014; Saleh et al. 2014).**

*Figure 10: It is very difficult to make out the fire perimeters on the two days. Please make these more distinct.*

We have adjusted line colors and styles throughout and added new figures that more clearly show the fire evolution/perimeters. We believe these changes enhance the interpretability of these data.

### Additional Changes Related to the Annotated Manuscript:

*Abstract: Line 3: Change “exceed” to “significantly higher than”*

**This change has been made**

*Pg. 29048, Line 22: What is meant by “non-developing” and “developing”?*

**“developing”= releases moist instability aloft**

**“non-developing” = forced convection analogous to fair weather cumulus clouds.**

**I have opted to keep it simple and changed the wording to read:**

***“Some pyroCu release significant moist instability aloft and thereby trigger deep convective clouds that sometimes grow into pyrocumulonimbus (pyroCb).”***

*Pg. 29049, Line 17: “examines” rather than “examine” (“a handful” is singular)*

**Changed**

*Pg. 29049, Line 24: “higher” “lower” might be more appropriate than “greater than, less than.”*

**Changed**

*Pg. 29051, Line 1: Please give fire coordinates.*

**Fire coordinates have been added**

*Pg. 29051, Line 20: “droplet” spelling*

**This section has been moved and modified. This discussion, with proper spelling, has been moved the Data and Methods section.**

*Pg. 29053, Line 6: Please give range from KMAX to Baldy.*

**The range is about 200 km. This has been added to the text, as has a figure showing the locations of the fires and radars.**

*Pg. 29053, Line 19: spell out (in reference to CBL)*

**changed**

*Pg. 29053, Line 25: what time? (what time was the balloon launch?)*

## Author Response

**2100 PDT, this has been added to the text.**

Pg. 29054, Line 25: Should this get a section number, like 2.4? (in reference to “lifted parcels” heading).

**This portion of the paper has been rearranged.**

Pg. 29056, Line 5: Please state the fire coordinates (Rocky Fire section)

**Coordinates added**

Pg. 29057, Line 29: degree symbol is preferred

**This discussion has been removed**

Pg. 29058, Line 10-15: What is the radar-fire range?

**~100 km. This has been added as has a map of the locations, including a distance scale**

Pg. 29058, Line 16: Do you mean echo tops or maximum reflectivity?

**We mean echo tops, and have changed the text.**

Pg. 29060, Line 26: delete "the"

**removed**

Pg. 29060, Line 27: pyroCu (replace pyroCi typo)

**corrected**

Pg. 29062, Line 1: extent not extend

**This line has been removed.**

Figure 2: The color scale labels here and elsewhere are apparently just the exponent part. This should be clarified.

**We have added a more thorough explanation of the lidar data in the Data and Methods section**

Figure 11: Please give time of radiosonde ascent.

**The times have been added to the radiosonde figures**

### **3. Tracked Changes**

Starting on next page....

1 **Environmental Controls on Pyrocumulus and**  
2 **Pyrocumulonimbus Initiation and Development**

3  
4 **N. P. Lareau<sup>1</sup> and C. B. Clements<sup>1</sup>**

5 (1){Fire Weather Research Laboratory, [Department of Meteorology and Climate Science,](#)  
6 San José State University, San Jose, California}

7 Correspondence to: N. P. Lareau (neil.lareau@sjsu.edu)

8

9 **Abstract:**

10 In this paper we present the first direct observational evidence that the condensation level  
11 in pyrocumulus and pyrocumulonimbus clouds can be significantly higher than the  
12 ambient lifted condensation level. In addition, we show that the environmental  
13 thermodynamic profile, day-to-day variations in humidity, and ambient wind shear all  
14 exert significant influence over the onset and development of pyroconvective clouds.  
15 These findings are established using a scanning Doppler lidar and mobile radiosonde  
16 system during two large wildfires in Northern California, the Bald and Rocky Fires. The  
17 lidar is used to distinguish liquid water from smoke backscatter during the plume rise,  
18 and thus provides a direct detection of plume condensations levels. Plume tops are  
19 subsequently determined from both the lidar and nearby radar observations. The  
20 radiosonde data, obtained adjacent to the fires, contextualizes the lidar and radar  
21 observations, and enables estimates of the plume ascent, convective available potential  
22 energy, and equilibrium level. A note worthy finding is that in these cases the Convective  
23 Condensation Level, not the Lifted Condensation Level, provides the best estimate of the  
24 pyrocumulus initiation height.  
25

Neil Lareau 2/11/16 3:40 PM  
Deleted: exceed

27 **1 Introduction**

28 Pyrocumulus (pyroCu) form when wildfire convective plumes rise to their condensation  
29 level and subsequently develop cumuliform cloud tops (American Meteorological  
30 Society 2015). The extent of pyroCu development depends on the relationships amongst  
31 atmospheric stratification, ambient moisture, and fire fluxes of heat and moisture (Potter  
32 | 2005; Luderer et al. 2006; 2009; Frietas et al. 2007). ~~Some~~ pyroCu release ~~significant~~  
33 moist instability aloft and thereby trigger deep convective clouds that sometimes grow  
34 into pyrocumulonimbus (pyroCb). Compared to their lesser counterparts, pyroCb posses  
35 glaciated cloud tops and can thus generate precipitation, downdrafts, and lightning  
36 (American Meteorological Society 2015). In exceptional cases, pyroCbs have been linked  
37 with extreme fire growth (Peterson et al. 2015), devastating firestorms (Fromm et al.  
38 2006), and even fire-induced tornados (Cunningham and Reeder 2009; McRae et al.  
39 2013).

40 In addition to their impact on fire behavior, pyroCu/Cb have garnered significant  
41 research attention due to their affect on vertical smoke transport, atmospheric chemistry,  
42 and cloud microphysics. For example, pyroCu can cause significantly deeper smoke  
43 injection than in dry convective cases (Frietas et al. 2007) and pyroCb are now  
44 recognized as the source of previously unexplained aerosol layers lofted in the lower  
45 stratosphere (Fromm and Servranckx 2003; Fromm et al. 2006; 2010). In addition,  
46 satellite and dual polarimetric radar observations of pyroCb show that the extreme  
47 aerosol loading results in high concentrations of small ice particles (Rosenfeld et al.  
48 2007), especially as compared to nearby clouds forming in smoke free air. The  
49 abundance of ice particles changes the radiative properties of the clouds and also favors  
50 atypical positive polarity lightning strokes (Rosenfeld et al. 2007; Lang et al. 2006;  
51 2012).

52 Despite the significant research on pyroCu/Cb microphysics, surprisingly little is  
53 known about the environmental controls on pyroCu development. To date only a handful  
54 | of studies explicitly examines the thermodynamic and kinematic structure of these cloud  
55 topped convective columns (Potter 2005, Trentman et al. 2006; Luderer et al. 2006; 2009;  
56 Frietas et al. 2007) and no studies include direct observations of pyroCu/Cb initiation. As  
57 a result, there is an open scientific debate regarding the plume condensation level, which

Neil Lareau 2/11/16 3:42 PM

**Deleted:** Non-developing pyroCu are relatively innocuous, whereas developing

60 is an important parameter for modeling smoke injection height and plume evolution  
61 (Frietas et al. 2007). Specifically, there are contrasting views in the literature about  
62 whether the plume condensation level is expected to be higher than or lower than the  
63 ambient lifted condensation level (LCL).

64 Potter (2005), for example, proposes that pyroCu/Cb should exhibit cloud bases  
65 lower than the ambient LCL due to the moisture released during combustion of woody  
66 fuels and from the evaporation of fuel moisture. Drawing on historical cases of  
67 pyroCu/Cb, radiosonde data, and theoretical considerations, he hypothesizes that the  
68 latent heat release may be the dominant factor in many moist-pyroconvective events. A  
69 limitation of this study is the anecdotal treatment of condensation levels, which are  
70 estimated, and the use of radiosonde observations that may not reflect the near fire  
71 environment.

72 In contrast to Potter (2005), Luderer et al. (2006; 2009) use high-resolution  
73 simulations and theoretical sensitivity calculations to conclude that “the combined effect  
74 of released moisture and heat from the fire almost always results in a higher cloud base  
75 compared to ambient conditions.” They also find that moisture released in combustion  
76 constitutes less than 10% of the pyroCu/Cb water budget with the remainder of the plume  
77 water resulting from entrained environmental air. While these modeled results are rather  
78 convincing, they lack clear observational support.

79 To that end, the only field observations that address plume moisture are from  
80 small scale grass fire experiments, where significant increases in water vapor mixing  
81 ratio are documented near the surface, but then decrease rapidly with height (Clements et  
82 al. 2006, 2007, Kiefer et al. 2012). While these observations are consistent with the  
83 dominant role of entrainment, such small-scale plumes may not be representative of deep  
84 convective plumes that extend into the upper troposphere or even lower stratosphere.

85 In this paper we present the first direct observations of condensation levels in two  
86 wildfire pyroCu/Cb cases. The fires, the Bald Fire and the Rocky Fire, were located in  
87 northern California, and observations were conducted on 2 August 2014 and 30 July  
88 2015, respectively (Fig. 1). The pyroCu cloud bases and plume rise dynamics were  
89 measured using a mobile atmospheric profiling system (Clements and Oliphant 2014)  
90 that included a scanning Doppler lidar and an upper-air radiosonde system which

Neil Lareau 2/11/16 3:46 PM

**Deleted:** greater

Neil Lareau 2/11/16 3:46 PM

**Deleted:** ess

Neil Lareau 2/10/16 2:58 PM

**Deleted:** N

Neil Lareau 2/3/16 3:09 PM

**Comment [1]:** Added an overview figure showing the locations of the fires and radars along with the regional topography.

94 provided thermodynamic profiles immediately upstream of the fire perimeters. From  
95 these data, our results clearly show that observed plume condensation levels are  
96 substantially higher than the ambient LCL. Additional aspects of the plume rise,  
97 including limiting factors on convective growth and the role of environmental moisture  
98 are also examined.

## 99 **2 Data and Methods**

Neil Lareau 2/9/16 2:57 PM

**Comment [2]:** Added a Data and Methods Section

### 100 **2.1 Lidar Data**

101 In this study, data from a Halo Photonics scanning Doppler lidar are examined (Pearson  
102 et al. 2009). The lidar emits a 1.5  $\mu\text{m}$  laser beam and records two range resolved  
103 quantities: (1) the attenuated backscatter coefficient ( $\text{m}^{-1} \text{sr}^{-1}$ ), which is a range corrected  
104 measure of backscattered energy, and (2) the Doppler velocity ( $\text{m s}^{-1}$ ). The lidar also  
105 reports the signal-to-noise ratio (SNR), which is useful for discriminating between  
106 meteorological targets and instrument noise. The lidar range is 9.6 km and the range-gate  
107 resolution is 18 m. Azimuth and elevation motors allow for scans of the full upper  
108 hemisphere and the lidar is level-mounted to the bed of a pickup truck, enabling rapid  
109 deployments to wildfires (Clements and Oliphant 2014).

#### 110 **2.1.1 Lidar Sensitivity**

111 Near-IR lidars are sensitive to aerosol, cloud droplets, and forest fire smoke. Due  
112 to these sensitivities numerous previous studies have used lidars to examine smoke layers  
113 and smoke plumes (Banta et al. 1992; Kovalev et al. 2005; Pahlow et al. 2005 Charland  
114 and Clements 2013; Lareau and Clements 2015).

115 Forest fire smoke typically exhibits a log-normal particle number distribution  
116 with a peak near  $.13 \mu\text{m}$  and a long tail extending towards coarser particles (Radke et al.  
117 1990, 1991; Banta et al. 1992; Reid and Hobbs 1998; Reid et al. 2005). The  
118 corresponding mass distributions are bimodal with peaks near  $.1$  and  $10 \mu\text{m}$  and a local  
119 minimum between 1 and  $3 \mu\text{m}$  (Radke et al. 1990, 1991; Reid et al. 2005). During intense  
120 forest fires, such as those in this study, additional “super-giant” aerosol with sizes  
121 sometimes exceeding 1 mm may also be prevalent (Radke et al. 1990, 1991; Reid et al.

122 2005). These aerosols are typically composed of large ash and soil particles, which may  
123 be scoured from the surface by strong fire-induced winds (Radke et al. 1991; Reid et al.  
124 2005; Kavouras et al. 2012).

125       The 1.5  $\mu\text{m}$  lidar beam interacts with the submicron smoke via Rayleigh  
126 scattering, the micron sized smoke via Mie scattering, and with the coarsest aerosol (e.g.,  
127 large ash, debris, etc.) via geometric optics. Using a radiative transfer model, Banta et al.  
128 (1992) showed that the attenuated backscatter coefficient due to the numerous small  
129 smoke particles was roughly comparable to the backscatter from the sparse large particles  
130 in a given volume. Similar behavior is expected with the lidar used in this study. In  
131 addition, based on our own experience, we expect significant attenuation for interactions  
132 with very coarse debris, especially near the base of smoke plumes.

133       Near-IR lidars also record high backscatter and rapid attenuation due to cloud  
134 droplets, making them an ideal tool for cloud base and cloud top detections (Hogan et al.  
135 2003; Winkler et al. 2009). In this study we leverage this attribute of the lidar to  
136 determine pyroCu cloud bases and edges in convective column. Similarly, Banta et al.  
137 (1992) used an IR lidar to identify pyroclouds in a wildfire smoke column.

### 138 **2.1.2 Lidar Scan Strategy**

139       The lidar was programmed to conduct “range-height indicator” (RHI) scans  
140 centered on the Bald Fire and Rocky Fire pyroconvective plumes. The scan azimuth  
141 angles were determined visually. During the Bald Fire the RHI elevation step was  $0.7^\circ$ ,  
142 whereas an elevation step of  $1^\circ$  was used during the Rocky Fire. Scans were conducted  
143 between the horizon and  $\sim 85^\circ$  in elevation, with a full RHI sweep taking  $\sim 1$  min during  
144 the Bald Fire and  $\sim 45$  sec during the Rocky Fire. Additional scan details, including the  
145 azimuth angles, are provided in the following case studies.

146       The lidar was also used to examine the velocity field near the fires and within the  
147 convective plumes. For example, the Doppler radial velocity data collected during the  
148 RHI scans are used to inspect the plume structure. These data have a resolution of 3-  
149 4  $\text{cm s}^{-1}$  over a range of  $\pm 19 \text{ m s}^{-1}$  (Pearson et al. 2009). In addition, conical scans were  
150 interspersed with RHI scans to generate vertical profiles of the horizontal wind using the  
151 “velocity-azimuth display” (VAD) technique (Browning and Wexler 1968). The VADs

Neil Lareau 2/2/16 3:50 PM  
Formatted: Indent: First line: 0.5"

152 use an elevation angle of 50° and span 360° in azimuth, taking about 1 minute to  
153 complete. The post-processed wind speed and direction from the VADs reflect the  
154 ambient winds above the lidar.

### 155 **2.1.3 Plume Edge Detection**

156 The lidar data are post-processed to determine plume boundaries and beam  
157 attenuation depth. The edge detection algorithm uses a combination of the lidar signal-to-  
158 noise ratio (SNR) and attenuated backscatter coefficient to isolate the plume. Similar  
159 approaches are presented in previous studies (Kovalev et al. 2005; Charland and  
160 Clements 2013). In our analysis, we first apply a 5<sup>th</sup> order Butterworth filter with a 5-  
161 point window to the SNR data along each lidar beam to eliminate some of the instrument  
162 noise. Next we record the radial location of maximum attenuated backscatter coefficient.  
163 Starting from that location we search inward along the beam for the first range gate  
164 where the SNR+1 drops below 1.01. This point is considered to be the leading plume  
165 edge. The same technique is performed searching outward along the beam to find the  
166 trailing plume edge. The trailing edge is considered to be the attenuation point provided  
167 the SNR+1 does not again exceed the threshold at some further distance. The SNR+1  
168 threshold of 1.01 was found to best discriminate between aerosol returns and background  
169 noise in our data sets, though other values (e.g., SNR+1=1.02) provide similar results.

170 To demonstrate the algorithm, Fig. 2 presents lidar data extracted from two  
171 elevation angles (10.2°, 46.7°) within a full RHI scan of Bald Fire convective column.  
172 The lower elevations beam (Fig. 2a) intersects the base of the smoke plume while the  
173 upper beam (Fig. 2b) hits the pyroCu. Of note, the SNR+1 associated with cloud is  
174 somewhat higher than in the smoke (1.105 vs. 1.089) and beam's attenuation is much  
175 more rapid, penetrating only 198 m into the cloud compared to 648 m into the smoke. In  
176 the following case studies we show that the sudden reduction in attenuation depth and  
177 increase in attenuated backscatter coefficient aloft are robust signatures of pyroCu  
178 formation.

179 **2.2 Radar Data**

180 Data from four National Weather Service (NWS) radars are used to examine plume  
181 structure. These 10-cm radars are sensitive to large ash and hydrometeors in the  
182 convective column but insensitive to cloud droplets and sub-micron smoke. Radars have  
183 been used in numerous wildfires studies (Banta et al. 1992; Hufford et al. 1998; Fromm  
184 et al. 2006; Rosenfeld et al. 2007; Jones and Christopher 2010a,b). Recently, dual-  
185 polarization radars have been used to examine the microphysics of wildfire plumes and  
186 clouds (Melnikov et al. 2008, 2009; Lang et al. 2014).

187 In this study we leverage three aspects of the NWS radars. First we examine the  
188 radar echo tops to estimate the maximum smoke injection height. The echo tops are the  
189 highest level at which the radar reflectivity exceeds 18 dbZ (Lakshmanan et al. 2013).  
190 Second we combine radar reflectivity from multiple radars to generate volume renderings  
191 of the pyroconvective plumes. These volumes are constructed by creating a gridded  
192 interpolant from all the available contemporaneous radar data. Data from the Medford,  
193 Reno, Beale, and Sacramento radars are combined for the Bald Fire, and from the Beale  
194 and Sacramento radars for the Rocky Fire. The radar locations relative to the fires are  
195 shown in Fig. 1.

196 Finally, we inspect the differential reflectivity ( $Z_{dr}$ ) data from the Medford, OR  
197 radar during the Bald Fire.  $Z_{dr}$  is the logarithmic ratio of the reflectivity from the  
198 horizontally and vertically polarized radar beams (Markowski and Richardson 2011).  
199 When  $Z_{dr}$  is large and positive it indicates the presence of large horizontal targets,  
200 including needle-like ash particles (Melnikov 2008, 2009). When  $Z_{dr}$  is near zero the  
201 targets are more spherical (e.g. hydrometeors), and when negative the targets are  
202 vertically oriented (e.g., graupel).

203 **2.3 Satellite Data**

204 Visible satellite observations from GOES-15 are used to characterize the presence of  
205 pyroCu above each fire. These data have a spatial resolution of 1 km and a nominal  
206 temporal resolution of 15 minutes, depending on the scan schedule. Data from the  
207 Moderate Resolution Imaging Spectroradiometer (MODIS) Terra and Aqua satellites are  
208 also used. These data include both true color visible images and fire-radiative power

Neil Lareau 2/10/16 3:36 PM  
**Formatted:** Indent: First line: 0.4", Line spacing: 1.5 lines

Neil Lareau 2/10/16 3:36 PM  
**Formatted:** Line spacing: 1.5 lines

Neil Lareau 2/10/16 4:27 PM  
**Formatted:** Subscript

Neil Lareau 2/11/16 10:33 AM  
**Formatted:** Justified, Indent: First line: 0.4", Line spacing: 1.5 lines

Neil Lareau 2/10/16 4:27 PM  
**Formatted:** Subscript

Neil Lareau 2/10/16 4:27 PM  
**Formatted:** Subscript

Neil Lareau 2/10/16 4:27 PM  
**Formatted:** Subscript

209 (FRP). The nominal resolution is 500 m. FRP is derived by differencing fire pixels from  
210 adjacent non-fire pixels using infrared radiance (Wooster 2002) and has been shown to  
211 provide high fidelity representation of fire activity during California wildfires (Koltunov  
212 et al. 2012; Peterson et al. 2015). FRP data from GOES are also examined.

#### 213 **2.4 Radiosonde Observation and Analysis**

214 Thermodynamic profiles were collected adjacent to both fires using a GRAW™  
215 GS-E radiosonde system. These sondes measure temperature, humidity, and wind from  
216 the surface to the tropopause, ascending at a rate of ~3 m s<sup>-1</sup>. The balloons were launched  
217 after sunset to avoid interfering with daytime fire-suppression aircraft operations, and as  
218 a result the temperature profiles include surface-based stable layers that are not  
219 representative of daytime conditions. To address this shortcoming, the afternoon  
220 temperature from the truck weather station is used to infer the convective boundary layer  
221 (CBL) depth using the “parcel method” (Holtzworth 1964).

222 The sonde data are used to examine the ambient condensation level by  
223 considering three lifted parcels (1) the most unstable (MU) parcel, (2) the mixed-layer  
224 (ML) parcel, and (3) the convective (CONV) parcel. The MU parcel is the parcel with the  
225 highest convective available potential energy (CAPE), whereas the ML parcel is based on  
226 the mean temperature and mixing ratio in the lowest 150 hPa. The CONV parcel reflects  
227 the surface temperature required for free convection based on the surface mixing ratio.  
228 The condensation level for each of these parcels is compared in the analyses below.

#### 230 **3 The Bald Fire**

231 The Bald Fire (40.9 N, 121.3 W) was started by lightning late on 31 July 2014. It was one  
232 of several lightning ignited fires in northern California and southern Oregon, including  
233 the adjacent Eiler Fire. The fire growth patterns on 1 and 2 August, determined from  
234 nightly U.S. Forest Service airborne infrared sensing (<http://nirops.fs.fed.us/>), are shown  
235 in Fig. 3. Based on these data, the fire consumed 7275 ha of mixed conifer forest during  
236 its first day, and by the end of the subsequent day had burned an additional 6821 ha. The

Neil Lareau 2/11/16 11:09 AM  
Formatted: Font:Times New Roman

Neil Lareau 2/11/16 11:09 AM  
Formatted: Font:Times New Roman

Neil Lareau 2/11/16 11:09 AM  
Formatted: Font:Times New Roman

craig clements 2/13/16 8:29 PM  
Deleted: ir

Neil Lareau 2/11/16 11:09 AM  
Formatted: Font:Times New Roman

craig clements 2/13/16 8:30 PM  
Deleted: of

239 weather conditions on both days featured afternoon high temperatures near 30° C,  
240 relative humidity of ~15 % and west winds gusting up to 6 m s<sup>-1</sup>.

241 During its rapid expansion on 2 Aug., the Bald fire developed a towering pyroCu  
242 that subsequently matured into pyroCb. Visible satellite data show the pyroCu initiation  
243 occurred at 1330 PDT, with continued cloud growth through mid-afternoon (Fig. 4a-d).  
244 At 1426 PDT the MODIS-Aqua satellite recorded a detailed image of the growing  
245 pyroCu, showing crisp cumuliform cloud features above the fire perimeter with more  
246 diffuse cloud elements extending to the northeast (Fig. 4e). The spreading cloud features  
247 were detrained from the primary updraft and then advected in southwesterly flow aloft.

248 The total FRP from the Bald Fire at the time of the MODIS-Aqua image was  
249 19700 MW summed over 30 fire pixels. The pixel maximum was 2258 MW, though the  
250 pyroCu obscures a substantial portion of the fire. For comparison, the earlier MODIS-  
251 Terra overpass at 1245 PDT yielded a maximum FRP of just 829 MW and a total FRP of  
252 3836 MW summed over 13 fire pixels. Clearly the fire experienced a rapid change in size  
253 and intensity during the early afternoon, coincident with the development of the pyroCu.

### 255 3.1 Lidar Observations

256 The truck-mounted Doppler lidar was situated ~7 km southwest of the fire where  
257 it conducted RHI scans of the windward edge of the developing pyroCu from 1350 to  
258 1532 PDT on 2 August. During this time, 95 RHI scans were completed, providing a time  
259 and space resolved measure of the plume evolution, including the height of the  
260 condensation level. The lidar location relative to the fire perimeter is indicated in Figs. 3  
261 and 4e. Figure 4f provides photograph from the lidar vantage point showing the  
262 windward edge of the cloud capped smoke column.

263 Figure 5 shows a sequence of lidar scans spanning the 5-minute period prior to the  
264 MODIS-Aqua overpass. These data are expressed as the logarithmic attenuated  
265 backscatter coefficient (hereafter backscatter) in units of m<sup>-1</sup> sr<sup>-1</sup>. Red and blue dots  
266 represent the leading plume edge and attenuation point, respectively, along each  
267 individual beam. The backscatter is due to smoke and debris in the lower portion of the  
268 plume (below 5500 m) and due to cloud droplets in the pyroCu aloft. The laser beam

Neil Lareau 2/2/16 4:15 PM

**Deleted:** The Bald Fire was started by lightning 31 July 2014 and subsequently developed a deep convective plume capped with pyroCu and then pyroCb on the afternoon of 2 August. Shortly after the pyroCu initiation (~1400 PDT) the afternoon MODIS overpass recorded a detailed image of the growing pyroCu, along with instantaneous observations of fire radiative power (FRP, Fig. 1a). The maximum FRP within the Bald Fire perimeter was 2645 MW, though the pyroCu, which interrupts the FRP computation, obscured much of the actively burning region.

Neil Lareau 2/4/16 9:59 AM

**Deleted:** vertical sector

Neil Lareau 2/4/16 9:56 AM

**Deleted:** smoke plume and

Neil Lareau 2/11/16 9:34 AM

**Deleted:** cumulus

Neil Lareau 2/11/16 9:34 AM

**Deleted:** cloud

Neil Lareau 2/4/16 10:02 AM

**Deleted:**

Neil Lareau 2/4/16 10:02 AM

**Deleted:** 1

Neil Lareau 2/4/16 10:02 AM

**Deleted:** b

Neil Lareau 2/11/16 9:34 AM

**Deleted:** towering

Neil Lareau 2/11/16 9:35 AM

**Deleted:** capped with pyroCu/Cb, and at times pileus clouds

Neil Lareau 2/4/16 10:02 AM

**Deleted:** The lidar scans from this location provide a detailed picture of the plume edge and aspects of the plume rise, including the condensation level.

Neil Lareau 2/4/16 10:48 AM

**Deleted:** 2

Neil Lareau 2/4/16 10:44 AM

**Deleted:** , for example,

Neil Lareau 2/4/16 10:53 AM

**Deleted:** during the plume rise

Neil Lareau 2/4/16 10:47 AM

**Deleted:** .

300 attenuates in both the smoke and the cloud water, but the cloud edge is marked by a  
301 distinct increase in the backscatter and more rapid attenuation. For example the distance  
302 between the leading plume edge (red dots) and the attenuation point (blue dots) tends to  
303 be much larger in the lower portion of the plume, whereas above 5500 m the attenuation  
304 occurs over just a few range gates. These aspects of the data give the pyroCu cloud  
305 returns a “crisper” edge.

306 While pyroCu were already present at the beginning of the scan sequence, the  
307 data show the development of a new cloud element. Figures 5a, b for example, show only  
308 a few points of rapid attenuation and high backscatter aloft, whereas starting at Fig. 5c a  
309 new, upright cloud edge is detected. This nascent pyroCu element then rapidly expands  
310 during the subsequent RHI scans, reaching a height of at least 8500 m before moving out  
311 of the lidar field of view (Fig. 5d-f). As we show in the radar analysis below, the actual  
312 plume top was as high as 12 km in the 10 minutes following these scans.

313 The scans, which were roughly parallel to the mean wind direction, also reveal  
314 that the plume experienced significant variations in tilt with time, alternating between  
315 windward (Fig. 5a) and rearward sloping geometries (Fig. 5f). In fact, the windward  
316 protrusion of the plume was as much as 2 km away from its base. Large coherent vortices  
317 are also apparent along the plume edge, especially in Fig. 5a,b as the “stair step” pattern  
318 in the plume edge detections. Based on the radial velocity data (not shown) the inward  
319 clefts in the plume edge correspond to enhanced flow into the plume and outward lobes  
320 reflecting flow towards the lidar. Vortices of this sort are a well-known feature of rising  
321 thermals and plumes and play a leading role in entrainment (Scorer 1957; Woodward  
322 1959).

323 Following the initial plume rise, sustained pyroCu were observed with the lidar  
324 until 1532 PDT, at which point the truck was relocated for safety reasons. To determine  
325 the plume condensation level, we aggregate data from all of the lidar scans during this  
326 period. From this larger data sample, Fig. 6a presents the time-maximum backscatter as a  
327 function of height and distance, and in Fig. 6b as a function of height only. In addition,  
328 Fig. 6c shows the computed percentiles (5, 50, and 95<sup>th</sup> percentiles) of the attenuation  
329 depth binned into 100 m intervals. Collectively, these data reinforce many of the aspects  
330 of the initial plume rise sequence discussed above. For example, there is a persistent

Neil Lareau 2/4/16 10:45 AM

**Deleted:** The backscatter is sensitive to micron-sized aerosol including smoke particles and liquid water droplets, and while the lidar beam ultimately attenuates in both, its attenuation is more rapid into cloud droplets. In addition, the signal-to-noise ratio (SNR) for cloud returns tends to be very high (>1.2), whereas it is somewhat lower in smoke and other aerosol. These aspects of the data make direct detection of the condensation level within the plume possible. Banta et al. (1992), for example, determined pyroCu boundaries using a subjective identification from lidar backscatter patterns, and more broadly, terrestrial lidars are regularly used to determine cloud base heights (e.g., Hogan et al. 2003)

Neil Lareau 2/4/16 10:56 AM

**Formatted:** Font color: Black

Neil Lareau 2/4/16 10:56 AM

**Deleted:** In the present case, condensation is first apparent within the developing convective column at ~5500 m MSL (all heights are MSL, above mean sea level, and hereafter just listed in meters), starting between 1419 and 1420 PDT (Fig. 2a,b). The cloud edge is marked by a distinct increase in the backscatter and more rapid attenuation giving the data a “crisper” edge that defines the pyroCu boundary. The nascent pyroCu then rapidly expands during the subsequent scans, obtaining a height of at least 8500 m by 14:24 PDT (Fig. 2e). The lidar range (9.6 km) limited the plume top detection, and as we show below the actual plume top was as high as 12 km.

Neil Lareau 2/9/16 2:42 PM

**Deleted:** eddies, or “ring vortices,”

Neil Lareau 2/16/16 10:36 AM

**Deleted:** (e.g., entrainment)

Neil Lareau 2/4/16 10:59 AM

**Deleted:** :

Neil Lareau 2/4/16 11:06 AM

**Deleted:** lidar

Neil Lareau 2/4/16 11:09 AM

**Deleted:** . For example, the plume went through many variations in “uprightness”, manifest as an envelope of plume edge detections (Fig. 3a). It is also readily apparent from these data that

372 transition in backscatter near 5500 m (blue line in Fig. 6a,b). Below this level, the  
373 backscatter approximately linearly decreases with height, consistent with the entrainment  
374 of clear air into an aerosol-laden plume. In contrast, at 5500 m the backscatter sharply  
375 increases (as does the SNR, not shown), corresponding to the condensation level and  
376 development of the pyroCu. The backscatter intensity remains high there and above due  
377 to the continued presence of liquid water.

378 The attenuation depth also shows a sharp transition at 5500 m (Fig. 6c). Below that  
379 level the median attenuation depth increases with height, which is again consistent with  
380 the dilution of the smoke plume via entrainment. At 5500 m the attenuation depth (across  
381 all percentiles) sharply decreases, converging towards a median value of ~200 m. The  
382 rapid attenuation aloft is consistent with the presence of liquid water drops and supports  
383 our interpretation that the change in backscatter intensity is due to condensation in the  
384 plume. From these data, we therefore conclude that the observed condensation level  
385 occurs very near 5500 m and was nearly constant throughout the 1.5 h observation period  
386 despite many changes in fire intensity.

### 387 3.2 Radar Analysis

388 Since the pyroCu cloud tops exceeded the lidar range the maximum smoke injection  
389 depth is obtained from the radar echo tops product from the NWS radar in Medford, OR  
390 (KMAX), which is ~200 km to the northwest. Figure 7a shows the time-maximum of the  
391 echo tops above the Bald Fire on 2 August. These data indicate that smoke reached  
392 altitudes in excess of 12 km, and thus the convective column rose an additional 3.5 km  
393 above the maximum height resolved in the lidar scans. The radar returns also show that  
394 the highest echo tops occur in a localized region above the fire perimeter where pyroCu  
395 were most prevalent. In contrast, the smoke layers without pyroCu correspond to plume  
396 heights closer to 6 km.

397 An additional interesting aspect of the radar data is the presence of deep echo tops  
398 southwest (e.g., upwind) of the infrared fire perimeter (solid contours, Fig. 7a). This  
399 observation is consistent with the periodic forward tilt of the plume as observed in the  
400 lidar backscatter (Figs. 5, 6). We hypothesize that the forward tilt relates to large-scale  
401 vortices that form as the plume penetrates through a stable layer at the top of the

Neil Lareau 2/9/16 3:38 PM

Deleted: green

Neil Lareau 2/9/16 3:39 PM

Deleted: turbulent

Neil Lareau 2/4/16 11:26 AM

Deleted: Notably, the condensation level was nearly constant throughout the 1.5 hr observation period despite many changes in fire intensity.

Neil Lareau 2/8/16 12:07 PM

Deleted: Plume Tops

Neil Lareau 2/10/16 4:41 PM

Deleted: the nearby

Neil Lareau 2/4/16 11:27 AM

Deleted: ational Weather Service WSR-88D

Neil Lareau 2/4/16 11:27 AM

Deleted: This 12-cm radar is sensitive to soot and ash, and thus provides high temporal resolution plume observations (c.f., Rosenfeld et al. 2007). Echo tops are derived from the radar's volume scan pattern as the highest level with reflectivity in excess of 18 dBz, which is nominally the clear air threshold.

Neil Lareau 2/11/16 9:41 AM

Deleted: that

Neil Lareau 2/16/16 10:40 AM

Deleted: radar

Neil Lareau 2/4/16 11:29 AM

Deleted: exceed

Neil Lareau 2/4/16 11:29 AM

Deleted: pyroCu

Neil Lareau 2/4/16 11:29 AM

Deleted: plume heights

Neil Lareau 2/10/16 4:43 PM

Deleted: pyrocumuli

Neil Lareau 2/9/16 3:41 PM

Deleted: pyrocumuli

Neil Lareau 2/10/16 4:43 PM

Deleted: plume

Neil Lareau 2/9/16 3:42 PM

Deleted: ring

Neil Lareau 2/9/16 3:50 PM

Deleted: CBL

428 boundary layer (Saunders 1961), and due to the deflection of the ambient flow around the  
429 plume.

430 Figure 7b shows the corresponding time series of the maximum radar echo tops.  
431 The pyroCu initiation at 1330 PDT, as shown in Fig. 4b, corresponds to a rapid rise in  
432 echo tops from 6500 m to 10000 m. Following the initial plume growth, the plume tops  
433 slowly rise until 1420 PDT at which point a second period of rapid plume growth occurs,  
434 pushing the convective column to heights above 12 km. The onset of this deep plume  
435 penetration closely corresponds to the lidar plume rise sequence shown in Fig. 6, as well  
436 as the MODIS-aqua image. The plume heights subsequently subside, remaining near 10  
437 km for the balance of the afternoon before diminishing more substantively at night.

438 A 3-D volume rendering of radar reflectivity from the Bald Fire at the time of  
439 maximum injection height (1429 PDT) reveals additional aspects of the plume structure  
440 (Fig 7c). The isosurfaces for 30, 28, 26, 24, and 18 dbZ are shown, along with the fire  
441 perimeters (red shading), lidar scan plane (black dots), lidar plume edge detections  
442 (yellow dots), and the lidar derived condensation level (green contour). These volume  
443 data show an expansive region of high reflectivity immediately above the fire perimeter.  
444 The reflectivity and plume height diminish towards the northeast, consistent with the fall  
445 out of the larger soot and ash particles in the downwind direction (e.g., southwest flow  
446 aloft). We note that since the radar is not sensitive to cloud droplets or micron sized  
447 smoke, it is possible that the cloud edges and some smoke reside outside of the radar  
448 volume rendering. It is also clear from these data that the lidar sees only the leading edge  
449 of the plume before attenuating in dense smoke and cloud water, consistent with the  
450 analyses presented above.

451 The shape of particles within the plume can be inferred by considering the  
452 differential reflectivity ( $Z_{dr}$ ) from the Medford, OR radar at different heights (Fig. 8).  
453 Three elevation angles are inspected (0.5, 1.5, and 2.4 deg.), intersecting the updraft core  
454 at heights of 4115, 7742, and 11009 m, respectively. The lowest scan shows very high  
455  $Z_{dr}$ , indicative of large, horizontally oriented particles, which is consistent with ash  
456 (Melnikov 2008, 2009; Lange et al. 2014) (Fig. 8a). In contrast, the mid elevation scan  
457 intersects the plume above the condensation level and shows a significant reduction in  
458  $Z_{dr}$ , with values between 0 and 2.5 in the updraft core (Fig. 8b). These values correspond

459 | to more spherical particles and small ice, suggesting the presence of large hydrometeors.  
460 | Finally the upper-most portion of the plume, at ~11 km, exhibits negative  $Z_{dr}$ , posing the  
461 | possibility of vertically oriented graupel particles (Fig. 8c).

### 462 | 3.3 Thermodynamic Analysis

463 | The lidar observed condensation level and radar estimated plume tops provide valuable  
464 | constraints on the plume structure when contextualized with atmospheric profiles  
465 | collected adjacent to the fire. Figure 9a, for example, shows data from a radiosonde  
466 | launched at 2100 PDT from ~15 km to the southwest of the fire (location shown in  
467 | Fig. 3).

468 | The sounding shows that the afternoon CBL extends from the surface (1364 m) to  
469 | ~4000 m and is capped by a pronounced stable layer. Within the CBL, the water vapor  
470 | mixing ratio is roughly constant at ~5 g kg<sup>-1</sup>, whereas above the CBL a layer of very dry  
471 | air is observed with a mixing ratio of only ~0.5 g kg<sup>-1</sup>. Further aloft, near 400 hPa, a layer  
472 | of higher humidity air, reflecting monsoonal moisture, is found. The height of the  
473 | tropopause is ~13 km.

474 | Relative to the observed profile, the “in cloud” profile is estimated by pseudo-  
475 | adiabatically lifting a parcel from the lidar observed condensation level at 5500 m. The  
476 | resulting parcel possesses 910 J kg<sup>-1</sup> of CAPE, which is an upper bound on the energy  
477 | available for buoyant ascent. The equilibrium level (EL) of the pyroCu parcel is 11,742  
478 | m, which is in close agreement with the radar estimated echo tops, but does not account  
479 | for the inertial overshoot of the parcel, which is likely reflected in the localized region of  
480 | radar plume heights exceeding 12 km (Fig. 7a).

481 | Also of note, the homogeneous freezing level (-38° C) in the plume profile occurs  
482 | at 10,158 m and the temperature at the EL is -52° C, indicating that the upper portion of  
483 | the cloud must be glaciated. As such, this particular pyroconvective cloud should be  
484 | classified as a pyroCb. In fact, pyroCb from other nearby fires on that day were known to  
485 | produce lightning as well as a significant and destructive fire-whirl (Muller and Herbster  
486 | 2014)

Neil Lareau 2/11/16 11:37 AM

Deleted: radiosonde data from

Neil Lareau 2/9/16 3:49 PM

Deleted: a sounding taken

Neil Lareau 2/10/16 4:49 PM

Deleted: The balloon was launched after sunset to avoid interfering with daytime fire-suppression aircraft operations, and as a result includes a surface-based stable layer that is not representative of daytime conditions. To address this shortcoming, the afternoon temperature (measured on the truck weather station) was used to infer the CBL depth using the “parcel method” (Holtzworth 1964).

Neil Lareau 2/10/16 4:50 PM

Deleted: adjusted

Neil Lareau 2/11/16 11:38 AM

Deleted: water vapor

Neil Lareau 2/10/16 4:51 PM

Deleted: convective available potential energy (

Neil Lareau 2/10/16 4:51 PM

Deleted: )

Neil Lareau 2/11/16 5:00 PM

Deleted: pyroconvective

### 504 3.3.1 Lifted Parcels

505 One of the main goals of this paper is to compare the observed plume properties with  
506 conventional estimates of condensational level and convective potential. To that end, in  
507 this subsection we consider each of the three lifted parcels described in Section 2.4 as  
508 representations of the observed plume. The parcel ascents are shown in Fig. 9b.

509 In this case, the MU parcel (red line, Fig 9b) originates in the CBL and produces an  
510 LCL of 4367 m, which is more than 1 km lower than the lidar observed condensation  
511 level. In addition, compared to the observed plume structure, the MU parcel possesses  
512 minimal CAPE and must overcome appreciable convective inhibition (CIN) before  
513 reaching its level of free convection. Similarly, the ML parcel encounters its LCL at 4641  
514 m, possesses almost no CAPE, and also must overcome appreciable CIN (cyan line, Fig.  
515 9b). The LCL for the ML parcel is higher than that of the MU parcel because the layer  
516 averaged mixing ratio is less than the maximum mixing ratio in the CBL.

517 Interestingly, the CONV parcel provides the best representation of the observed  
518 plume (dark blue line, Fig. 9b). In this case the surface mixing ratio is  $5.2 \text{ g kg}^{-1}$  and the  
519 corresponding convective condensation level (CCL) is found at 5549 m, which is very  
520 close to the lidar derived 5500 m. Commensurately, the EL and CAPE for the CONV  
521 parcel are also close to the observed values. The convective temperature, which is the  
522 surface temperature that must be reached to support convection, is  $36.4^\circ \text{ C}$ . The high  
523 temperature for the day was  $29^\circ \text{ C}$ , making surface based convection extremely unlikely  
524 outside of the fire modified environment.

525 From these analyses it is clear that the plume condensation level is substantively  
526 higher than the ambient LCL, supporting the results of Luderer et al. (2006; 2009).  
527 Further, using the CCL, not the LCL, and assuming that the fire readily exceeds the  
528 convective temperature, provides the best representation of the plume condensation level  
529 in this case. This is a potentially useful diagnostic for forecasters and fire managers. It  
530 should be noted, however, that the CONV parcel, and its associated dry-adiabat up to the  
531 CCL (dark blue line, Fig. 9b), does necessarily reflect the actual properties of the lower  
532 plume. Rather, the plume must be superadiabatic near its base, cooling largely due to  
533 entrainment as it decays towards adiabatic ascent further aloft (Emanuel 1994;  
534 Trentmann et al. 2006; Frietas et al. 2007).

Neil Lareau 2/10/16 4:55 PM

Deleted: potential

Neil Lareau 2/10/16 5:05 PM

Deleted: , each of which

craig clements 2/15/16 8:32 AM

Deleted: is

Neil Lareau 2/11/16 9:46 AM

Deleted: .

Neil Lareau 2/10/16 4:58 PM

Formatted: Indent: First line: 0.3"

Neil Lareau 2/10/16 5:06 PM

Deleted: 5500 m

Neil Lareau 2/10/16 4:58 PM

Deleted: .

Neil Lareau 2/10/16 4:59 PM

Deleted: exceeds

Neil Lareau 2/10/16 4:59 PM

Deleted: .

Neil Lareau 2/10/16 5:00 PM

Deleted: *Convective Parcel*: The convective condensation level (CCL) is the height at which the environment temperature profile supports saturation for the observed near-surface mixing ratio.

Neil Lareau 2/10/16 5:03 PM

Deleted: observed condensation level of

Neil Lareau 2/11/16 9:47 AM

Deleted: convective

Neil Lareau 2/11/16 9:47 AM

Deleted: ~

Neil Lareau 2/10/16 5:03 PM

Deleted: .

Neil Lareau 2/10/16 5:04 PM

Deleted: convective temperature and the associated adiabat up to the CCL do not

556

## 557 4 The Rocky Fire

558 The Rocky Fire (38.9° N, 122.5° W) started late on 29 July 2015 (cause unknown) in the  
 559 coastal range of northern California and burned in complex terrain through fuels  
 560 consisting of grass, brush, and conifers (Figs. 1, 10). The U.S. Forest Service NROPS  
 561 fire perimeters show that the fire burned 3356 ha during the first day, and then consumed  
 562 another 3153 ha on 30 July, the day of our observations. The fire growth on the 30<sup>th</sup> was  
 563 complex, expanding along multiple flanks (Fig. 10). Notably the first day's fire growth,  
 564 while rapid, did not generate pyroCu, whereas the second day did (Fig. 11). In addition,  
 565 compared to the long-lived Bald Fire pyroCu/Cb, the Rocky Fire plumes were transient,  
 566 repeatedly forming and dissipating in rapid succession. In this section we examine the  
 567 structure of these transient pyroCu along with the environmental conditions affecting  
 568 their evolution.

### 569 4.1 Lidar Observations

570 Lidar RHI scans were conducted between 1545 and 2008 PDT from an already  
 571 burned area within the Rocky Fire perimeter (Fig. 10). This location allowed for scans of  
 572 four separate pyroCu plumes rising from the complex fire perimeter. A total of 267 RHI  
 573 scans were performed.

574 PyroCu were first observed with the lidar starting at ~1600 PDT rising from the  
 575 northwest flank of the fire (319° azimuth, scan path #1 in Fig. 10). Figure 12 shows a  
 576 sequence of photographs (top panels) and contemporaneous lidar scans (bottom panels)  
 577 detailing the onset and expansion of this cloud topped plume. The plume was initially  
 578 observed as it penetrated through a stable layer at the top of the CBL, evident as a lateral  
 579 smoke layer at ~2600 m in the backscatter data and as a diffuse haze in the photographs.  
 580 During this time a thin pileus cloud accompanied the developing pyroCu and the lidar  
 581 cloud returns were limited to a few points near the plume top (Fig. 12f).

582 By 16:03 PDT, however, a distinct cumuliform cloud had developed (Fig. 12b)  
 583 and the lidar backscatter showed a commensurate increase in intensity and attenuation  
 584 along the pyroCu edge (Fig. 12g). Based on these data the cloud base was at ~4200 m.

Neil Lareau 2/4/16 4:38 PM

**Deleted:** In this section we explore the impact of limiting processes on pyroCu development during the Rocky Fire.

Neil Lareau 2/8/16 1:25 PM

**Deleted:** on

Neil Lareau 2/11/16 12:14 PM

**Formatted:** Superscript

Neil Lareau 2/4/16 4:41 PM

**Deleted:** Compared to the long-lived Bald Fire pyroCb, the Rocky Fire plumes were less vertically developed and more transient, persisting only for a few 10s of minutes before dissipating.

Neil Lareau 2/8/16 1:30 PM

**Deleted:** 15:55

Neil Lareau 2/8/16 1:00 PM

**Deleted:** active

Neil Lareau 2/16/16 10:55 AM

**Deleted:** e

Neil Lareau 2/10/16 5:17 PM

**Deleted:** ~

598 The subsequent scans show the rapid pyroCu development, and by 1609 PDT cloud  
599 edges were detected as high as 7500 m. Interestingly, soon thereafter the pyroCu  
600 detrained from the convective column and dissipated (not shown).

601 Another pyroCu event at 1800 PDT is detailed in Fig. 13 corresponding to a lidar  
602 azimuth of 86° (scan path #3 in Fig. 11). This plume initiated ~2.5 km east of the lidar  
603 location. As in the previous case, the rapidly growing plume was first recorded as it rose  
604 through the boundary layer top, now at ~2300 m, and expanded into the free troposphere  
605 (Fig. 13a,e). Subsequent scans revealed the onset of pyroCu with a condensation level of  
606 4200 m, which is unchanged from the earlier Rocky Fire pyroCu event detailed in Fig.  
607 12. In this case, however, the cloud top was not as well documented because attenuation  
608 at the cloud base shielded the lidar view of the upper plume.

609 The photographs detailing the plume rise show changes in smoke colour near the  
610 base of the convective column (Fig. 13a-d). For example, at 1805 PDT the smoke is a  
611 dark gray (Fig. 13a), whereas later the smoke is increasingly white (Fig. 13d). We believe  
612 the change in smoke coloration is associated with changes in the completeness of  
613 combustion: flaming combustion produces smoke dominated by black carbon aerosols,  
614 whereas smoldering combustion generates more organic carbon aerosol, which more  
615 effectively backscatter sunlight and appear whiter (Bellouin 2014; Saleh et al. 2014).

616 An additional aspect of the observed plume rise is the relationship between the  
617 updraft strength and the ambient wind. This relationship is examined in Fig. 14, which  
618 displays VAD wind profiles (Fig. 14 a,b) and RHI radial velocities, detailing the plume  
619 structure (Fig. 14c-e). The wind profiles show significant shear over the lowest 2 km of  
620 the atmosphere. Strong (5-7 m s<sup>-1</sup>) northwesterly winds near the surface transition to  
621 weak flow at the boundary layer top (0-1 m s<sup>-1</sup> near 2300 m), then reverse to easterly flow  
622 aloft (Fig. 14a,b). The observed near-surface wind speed maximum is atypical in the  
623 atmospheric boundary layer and “adverse” wind profiles of this character have previously  
624 been linked to blow-up fires (Byram 1954).

625 Compared to the ambient wind, the flow within the plume is characterized by  
626 much stronger velocities (Fig. 14c,d). For example, outbound speeds in excess of 15 m s<sup>-1</sup>  
627 are recorded at numerous locations within the plume at 1809 PDT. The actual updraft  
628 speed likely exceeds these values since the radial velocity data only reflect the projection

Neil Lareau 2/8/16 12:12 PM

Deleted: second...other pyroCu grov ... [1]

Neil Lareau 2/4/16 4:46 PM

Deleted: e...observed plume rise is is ... [2]

671 of the updraft onto the oblique lidar beam. Significant downdrafts are also observed in  
672 the upper portion of the plume, especially at 1813 PDT (blue shading, Fig. 14c,d).

673 The RHI velocity data also show that the strength of the updraft diminished with  
674 time. For example, comparative histograms demonstrate that strong outbound velocities  
675 were both higher and more common at 1809 than 1813 PDT (Fig. 14e). This observation  
676 is consistent with the change in smoke coloration described above: flaming combustion is  
677 likely to produce stronger updrafts due to more rapid heat release.

678 Changes in plume geometry also accompany the reduction in updraft strength.  
679 The plume is at first mostly upright (Fig. 14c) and later becomes more sheared (Fig. 14d).  
680 Specifically, the leading plume edge becomes tilted downwind within the boundary layer  
681 while the upper portion of the plume bends back towards the observing location. Based  
682 on these data, we hypothesize that as the fire's updraft weakens it becomes more  
683 susceptible to the ambient shear. The role of wind shear as a limiting factor in plume  
684 development is further discussed below.

685 A more robust examination of the plume condensation level during the Rocky  
686 Fire's multiple pyroCu events is presented in Fig. 15. These analyses leverage the  
687 aggregated data from all of the RHI scans on 30 July. Unsurprisingly, the time-maximum  
688 backscatter exhibit a sharp transition near 4200 m (Fig. 15a, b), as was indicated in the  
689 earlier plume rise sequences (Figs. 12, 13). Below 4200 m the backscatter decays roughly  
690 linearly with height, and above that level the backscatter converges to a value of near  $-4$   
691  $\text{m}^{-1} \text{sr}^{-1}$  (Fig. 15b). Likewise, the attenuation depth linearly *increases* from the surface up  
692 to 4200 m, then abruptly decreases to a median depth of  $\sim 200$  m. This pattern is  
693 consistent with the dilution of the smoke plume by entrainment and the onset of  
694 condensation aloft. Importantly, these analyses are remarkably similar to those during the  
695 Bald Fire suggesting a clear lidar signature of pyroCu onset. Moreover, the condensation  
696 level is once again found to be constant throughout the observing period, indicating that  
697 ambient atmospheric conditions rather than variations in water released during  
698 combustion likely control its height.

craig clements 2/15/16 8:45 AM

Deleted: is

Neil Lareau 2/8/16 11:40 AM

**Deleted:** Compared to the ambient winds, the radial velocities measured within the plume are large, with peak values in excess of  $12 \text{ m s}^{-1}$  (Fig. 9). In fact, assuming that the flow within the plume is parallel to the plume centerline, which is semi-objectively determined for each scan, the maximum updraft strength is estimated to be in excess of  $\sim 18 \text{ m s}^{-1}$  at 1808 PDT. Thereafter, the updraft strength diminishes and the plume becomes increasingly laid over. For example, the plume is initially inclined at  $\sim 60$  degrees from the horizontal (Fig 9a), but just 5 minutes later is inclined at only 45 degrees (Fig. 9f). In fact, a short time later the plume ceased to penetrate through the boundary layer top and the pyroCu subsequently dissipated (not shown). We hypothesize that the weakening updraft makes the plume more susceptible to the environmental wind shear, leading to increasing plume tilt with time. Also of note, the reversed flow aloft tends to sweep a portion of the plume back towards the lidar, which separates the upper plume from the convective column rising through the boundary layer.

Neil Lareau 2/8/16 1:06 PM

Deleted: in the thermodynamics section

Neil Lareau 2/11/16 12:11 PM

Formatted: Font:Italic

## 726 4.2 Radar Analysis

727 Radar data are again used to estimate the maximum smoke injection depth. The Rocky  
728 Fire was within ~100 km of both the Sacramento (KDAX) and Beale Air Force Base  
729 (KBBX) NWS radars (Fig. 1), and data from both sites are in agreement.

730 The maximum echo tops (from KDAX) occur between 7000 m and 7500 m,  
731 consistent with the lidar cloud detections (Fig. 16a). The spatial pattern of echo tops  
732 indicate that plumes of similar height developed on all of the expanding flanks of the fire.  
733 Interestingly, the corresponding time series demonstrates the plume transience, showing  
734 rapid variations in plume height throughout the late afternoon (Fig. 16b). Each spike  
735 corresponds to a short-lived pyroCu with durations ranging from 10-30 minutes. Satellite  
736 data confirm the episodic nature of these plumes (not shown).

737 The variability in echo tops is also due to the presence of multiple updrafts. For  
738 example, a volume rendering of the reflectivity data at 1609 PDT shows the two distinct  
739 updrafts associated with the complex fire perimeter (Fig. 16c). The narrow updraft rising  
740 from the northwestern flank of the fire is the same plume shown in Fig. 12, and the lidar  
741 plume detections agree well with the radar data (yellow dots, Fig 16c). A second broader  
742 plume rises from the north and northeastern flanks of the fire at the same time. Above  
743 5000 m the upper portions of both plumes are tilted to the north-northwest due to  
744 southeasterly flow in that layer. Later in the fire's evolution the plume growth shifted  
745 towards the east and southeast (not shown).

## 746 4.3 Thermodynamic Analysis

747 The Rocky Fire pyroCu development is interesting in that the thermodynamic  
748 environment theoretically supports much deeper convection than was observed. Using  
749 radiosonde data from ~15 km southwest of the fire at 2105 PDT, Fig. 17a shows that  
750 moist adiabatic ascent from the observed 4200 m cloud base would generate 2035 J kg<sup>-1</sup>  
751 of CAPE and that the plume equilibrium level would be ~13 km, impinging on the  
752 tropopause. The radar and lidar data indicate, however, that the plumes ascended to no  
753 higher than ~7.5 km, corresponding to plume top temperature of -20° C. As such, these  
754 clouds are best classified as pyroCu, and never developed as deep pyroCb.

Neil Lareau 2/10/16 5:23 PM

Deleted: -

Neil Lareau 2/8/16 12:07 PM

Deleted: Plume Tops

Neil Lareau 2/8/16 11:44 AM

Deleted: Since definitive lidar detection of the plume tops was not possible, radar

Neil Lareau 2/9/16 4:33 PM

Deleted: is

Neil Lareau 2/9/16 10:02 AM

Deleted: range

Neil Lareau 2/9/16 10:02 AM

Deleted: , and the data from both sites are in good agreement. As such, here we show only the results from KDAX echo tops product (Fig. 10).

Neil Lareau 2/8/16 9:45 PM

Deleted: radar echoes

Neil Lareau 2/8/16 9:45 PM

Deleted:

Neil Lareau 2/8/16 11:57 AM

Deleted: 5

Neil Lareau 2/8/16 11:57 AM

Deleted: 80

Neil Lareau 2/8/16 11:57 AM

Deleted: during the first Rocky Fire pyroCu event

Neil Lareau 2/8/16 1:09 PM

Deleted: Relative to the fire perimeters,

Neil Lareau 2/8/16 12:00 PM

Deleted: the

Neil Lareau 2/8/16 1:10 PM

Deleted: local

Neil Lareau 2/8/16 1:09 PM

Deleted: plume

Neil Lareau 2/8/16 9:47 PM

Deleted: maxima

Neil Lareau 2/8/16 9:48 PM

Deleted: coincide with portions of the fire that

Neil Lareau 2/8/16 1:09 PM

Deleted: ed

Neil Lareau 2/8/16 1:09 PM

Deleted: most rapidly on 30 July.

Neil Lareau 2/8/16 1:10 PM

Deleted: Specifically, the first convec ... [3]

Neil Lareau 2/10/16 5:30 PM

Deleted: lidar, and visual observations

Neil Lareau 2/16/16 11:03 AM

Deleted: all

789 What then limits the growth? There appear to be two related limiting factors in the  
790 plume rise: (1) wind shear, and (2) dry air entrainment. The lidar wind profiles, presented  
791 above in Fig. 14, indicate significant wind shear between the CBL and free troposphere.  
792 This wind shear is also apparent in the radiosonde wind profile, which shows a 180-  
793 degree wind shift at 2300 m (wind barbs and hodograph Fig 17a). The flow below this  
794 level is from the west-northwest, whereas the flow above, and extending up to ~7 km, is  
795 from the east-southeast. The layer of southeasterly flow is associated with a surge of  
796 monsoonal moisture.

Neil Lareau 2/9/16 4:37 PM  
Deleted: entrainment of ...ry air into ... [4]

797 A second layer of significant wind shear at 7000 m separates the monsoon flow  
798 from southwesterly flow in the upper troposphere. This shear also coincides with a rapid  
799 decrease in dew point temperature, and thus relative humidity. It is notable then that the  
800 maximum echo tops occur only about 500 m above the upper shear layer. Visual  
801 observations throughout the afternoon and early evening suggest this shear zone affected  
802 the pyroCu development, tending to sweep the upper portion of the cloud away from the  
803 updraft core. The detraining upper portions of the cloud subsequently developed ragged  
804 and wispy edges indicative of dry air entrainment as opposed to the crisp crenellations of  
805 growing cumulus congestus.

Neil Lareau 2/9/16 10:59 AM  
Deleted: In fact, visual and...Visual ... [5]

806 The effect of the wind shear on a buoyant parcel is easily visualized by examining  
807 the ascent track of the radiosonde, which rose at a mean rate of 2.7 m s<sup>-1</sup> (Fig. 17b). The  
808 ambient shear causes a pronounced zigzag pattern that is clearly detrimental to sustained  
809 upright convection despite the substantive CAPE. This result is not surprising in that  
810 CAPE is known to overestimate convective development and updraft strength  
811 (Markowski and Richardson 2011).

Neil Lareau 2/9/16 10:58 AM  
Deleted: In addition, when the full column is considered, the two shear layers combine to create a zigzag wind profile...he effect ... [6]

812

Neil Lareau 2/8/16 12:48 PM  
Formatted: Font color: Black, Superscript

### 813 4.3.1 Lifted Parcels

814 Despite their limited vertical development, the Rocky Fire pyroCu provide  
815 additional support for the hypothesis that the plume condensation level occurs above the  
816 ambient LCL. Following the same procedures described for the Bald Fire we examine  
817 three convective parcels, the ascents of which are shown in Fig. 18. The LCLs for the  
818 MU and ML parcels are 3503 m and 3768 m, respectively (red and cyan lines, Fig. 18).

Neil Lareau 2/9/16 11:04 AM  
Deleted: ...the Rocky Firese...pyroC... [7]

856 Both of these lifted parcels must overcome modest CIN to reach their level of free  
857 convection. In contrast, the computed CCL of 4250 m is much closer to the lidar  
858 observed condensation level at ~4200 m. The corresponding convective temperature is  
859 ~43° C, which is higher than the observed daytime temperature of 39° C. These results,  
860 like those from the Bald Fire, again suggest that the CCL is a useful parameter for  
861 estimating pyroCu/Cb convective initiation heights.

Neil Lareau 2/10/16 5:35 PM

Deleted: .

#### 862 4.4 Fire Radiative Power and Environmental Moisture

863 Figure 19a shows the GOES-15 and MODIS FRP in for the Rocky Fire on 29-30  
864 July 2015. From these data it is clear that the diurnal cycle of fire intensity is similar  
865 during the first two days of fire growth, with peak FRP values near 1500 MW in the late  
866 afternoon and fire activity extending into the late evening. Interestingly, despite  
867 comparable fire intensity, pyroCu were not observed on the 29th but were widespread on  
868 the 30<sup>th</sup>.

Neil Lareau 2/10/16 5:35 PM

Deleted: 2... shows the GOES-15 and ... [8]

869 To better understand this disparity, Fig. 19b-e compares the ambient  
870 meteorological conditions between days. These data are from a weather station just  
871 outside the fire perimeter, the location of which is shown in Fig. 10 (data obtained from  
872 MesoWest, Horel et al. 2002), and the 1700 PDT upper air soundings at Oakland  
873 International Airport (KOAK, location shown in Fig. 1). The high temperature on both  
874 days was ~39° C and afternoon winds were from the west with peak gusts near 6 m s<sup>-1</sup>.  
875 The relative humidity was higher on the 30<sup>th</sup> than the 29<sup>th</sup>.

Neil Lareau 2/11/16 12:22 PM

Formatted: Superscript

Neil Lareau 2/11/16 12:24 PM

Deleted: ...Fig. 12

... [9]

876 Figures 19d,e show the time series of the water vapor mixing ratio and the  
877 differences in the relative humidity from the KOAK soundings for two afternoons. From  
878 these data it is apparent that the onset of pyroCu on 30 July corresponds to the arrival of  
879 much higher humidity air, both at the surface and aloft. For example, the mixing ratio  
880 increases from 4.5 g kg<sup>-1</sup> to 8 g kg<sup>-1</sup> while the relative humidity at 5500 m jumps from  
881 7% to 66%. The corresponding change in the CCL is substantial, dropping from 5848 m  
882 on 29<sup>th</sup> to 4267 m on the 30<sup>th</sup>. Since the fire intensity was similar on both afternoons it is  
883 likely that reduction in the height of CCL due to the influx of monsoon moisture was the  
884 driving factor in pyroCu formation. These observations support the conclusions of

Neil Lareau 2/11/16 12:43 PM

Formatted

... [10]

Neil Lareau 2/11/16 12:48 PM

Deleted: s...a...he time series of the ... [11]

Neil Lareau 2/11/16 12:50 PM

Deleted: remained ...as similar on b ... [12]

Neil Lareau 2/11/16 12:49 PM

Formatted: Superscript

932 Luderer et al. (2006; 2009) that environmental moisture, not water released in  
933 combustion, is the primary control on pyroCu development.  
934

## 935 5 Summary and Conclusions

936 The observations presented in this paper demonstrate that plume condensation levels  
937 can exceed the height of the ambient LCL, sometimes substantially. For example, during  
938 the Bald Fire the plume condensation level was more than 1 km higher than the  
939 environmental LCL. As such, we conclude that the LCL should not be used, as it has  
940 been, as a parameter for assessing pyroCu/Cb potential outside of the limiting case where  
941 the CCL and LCL coincide, which is to say that widespread convective clouds are  
942 possible. While our observational results span a limited portion of the parameter space,  
943 they nonetheless provide strong support for the modeling results of Luderer et al. (2006;  
944 2009) and Trentman et al. (2006), and seemingly contradict the results of Potter (2005).

945 While the CCL and the corresponding moist adiabatic ascent provide a useful  
946 approximation for plume properties, other factors must also be considered. Specifically,  
947 CAPE alone cannot determine the convective outcome. Our results from the Rocky Fire  
948 show, for example, that ambient wind shear and dry air entrainment can significantly  
949 curtail the convective development even in an environment that might otherwise support  
950 deep pyroCb. In addition, our results show that the change in environmental humidity,  
951 often in the form of a monsoonal surge, exerts a significant influence over the onset of  
952 pyroCu/Cb by raising or lowering the height of CCL. These results suggest that the  
953 moisture release during combustion is of secondary importance, at least in these observed  
954 cases.

955 While our results mark an advance in understanding pyroCu/Cb development  
956 there is a clear need for new measurement and modeling investigations of pyroconvective  
957 clouds. Future field campaigns should include observations of the ambient environment  
958 (e.g. radiosondes, CBL properties), the lower plume structure (temperature, moisture, and  
959 momentum fluxes), and cloud properties (e.g. liquid and ice water path, particle size  
960 distributions, etc.). These data should subsequently inform physical fluid dynamical  
961 models in order to investigate aspects of plume dynamics that may not be observable.  
962 Some potential avenues for obtaining these observations include dropsondes from

Neil Lareau 2/11/16 12:45 PM  
Formatted: Justified

Neil Lareau 2/11/16 12:57 PM  
Deleted: new, more complete observations of pyroconvective clouds.

Neil Lareau 2/11/16 12:58 PM  
Deleted: measurement

Neil Lareau 2/11/16 1:00 PM  
Deleted: simultaneous

Neil Lareau 2/11/16 1:01 PM  
Deleted: plume

Neil Lareau 2/11/16 1:01 PM  
Deleted: moisture

Neil Lareau 2/11/16 1:01 PM  
Deleted: , and cloud microphysics

Neil Lareau 2/11/16 1:03 PM  
Deleted: In addition, one key question in the plume rise dynamics is to what extent lofted debris affects buoyancy

Neil Lareau 2/11/16 1:03 PM  
Deleted: data

974 | aircraft, surface and aircraft based dual-polarization radars, unmanned aerial vehicles,  
975 | and dual-Doppler lidar deployed during large-scale prescribed burn experiments where  
976 | the fuel loading and extent of combustion is known or can be determined after the fact.

977

#### 978 **Author Contributions**

979 | C.C. conceived of the field program, N.L. and C.C. conducted the field measurements,  
980 | and N.L. led the data analysis and writing.

981

#### 982 **Acknowledgements**

983 | The lidar and radiosonde data are available upon request from the authors. All  
984 | other data sources are publically available. This research is supported under grant AGS-  
985 | 1151930 from the National Science Foundation. Christopher C. Camacho contributed to  
986 | the field observations during the Rocky Fire.

Neil Lareau 2/11/16 5:01 PM

Deleted: doppler

988 **6 References**

989 American Meteorological Society: "Pyrocumulus". Glossary of Meteorology. [Available  
990 online at <http://glossary.ametsoc.org/wiki/Pyrocumulus>], cited 2015.

991 American Meteorological Society: "Pyrocumulonimbus". Glossary of Meteorology.  
992 [Available online at <http://glossary.ametsoc.org/wiki/Pyrocumulonimbus>], cited 2015.

993 Banta, R. M., Olivier, L. D., Holloway, E. T., Kropfli, R. A., Bartram, B. W., Cupp, R.  
994 E., and Post, M. J.: Smoke-column observations from two forest fires using Doppler  
995 lidar and Doppler radar. *J. Appl. Meteorol.*, 31, 1328-1349,  
996 doi: [http://dx.doi.org/10.1175/1520-0450\(1992\)031<1328:SCOTF>2.0.CO;2](http://dx.doi.org/10.1175/1520-0450(1992)031<1328:SCOTF>2.0.CO;2), 1992.

997 [Bellouin, N.: Aerosols: The colour of smoke. \*Nature Geoscience\*, 7, 619-620.](#)  
998 [doi:10.1038/ngeo2226, 2014.](#)

999 [Browning, K. A., and Wexler, R.: The determination of kinematic properties of a wind  
1000 field using Doppler radar. \*J. Appl. Meteorol.\*, 7, 105-113, doi: 10.1175/1520-  
1001 0450\(1968\)007<0105:TDOKPO>2.0.CO;2, 1968](#)

1002 [Byram, G. M.: Atmospheric conditions related to blowup fires. \*Sta. Pap. 35. Asheville,\*  
1003 \*NC: US Department of Agriculture, Forest Service, Southeastern Forest Experiment\*  
1004 \*Station. 1954.\*](#)

1005 [Charland, A. M., and Clements, C. B.: Kinematic structure of a wildland fire plume  
1006 observed by Doppler lidar. \*J. Geophys. Res.\* 118, 3200-3212, doi: 10.1002/jgrd.50308,  
1007 2013.](#)

1008 [Clements, C. B., B.E. Potter, S. Zhong: \*In situ\* Measurements of Water Vapor, Heat and CO<sub>2</sub>  
1009 Fluxes within a prescribed Grass Fire. \*International Journal of Wildland Fire\*, 15\(3\),  
1010 299-306,2006.](#)

1011 [Clements, C. B., S. Zhong, S. Goodrick, J. Li, X. Bian, B.E. Potter, W. E. Heilman, J.J. Charney,  
1012 R. Perna, M. Jang, D. Lee, M. Patel, S. Street and G. Aumann: Observing the Dynamics of  
1013 Wildland Grass Fires: FireFlux- A Field Validation Experiment. \*Bull. Amer. Meteor. Soc.\*,  
1014 88\(9\), 1369-1382, 2007.](#)

1015 Clements, C. B., and Oliphant, A. J.: The California State University mobile atmospheric  
1016 profiling system: A facility for research and education in boundary layer meteorology.  
1017 *Bull. Amer. Meteor. Soc.* **95**, 1713-1724, doi: [10.1175/BAMS-D-13-00179.1](http://dx.doi.org/10.1175/BAMS-D-13-00179.1), 2014.

1018 Cunningham, P., and Reeder, M. J.: Severe convective storms initiated by intense  
1019 wildfires: Numerical simulations of pyro-convection and pyro-tornadogenesis.  
1020 *Geophys. Res. Lett.*, 36, L12812, doi:[10.1029/2009GL039262](http://dx.doi.org/10.1029/2009GL039262), 2009.

1021 Emanuel, K. A.: Atmospheric convection. Oxford University Press., 580 pp, 1994.

Neil Lareau 2/11/16 10:32 AM

Formatted: Font:Not Italic

Neil Lareau 2/11/16 10:32 AM

Formatted: Font:Not Italic

craig clements 2/13/16 8:16 PM

Formatted: Normal, Indent: Left: 0",  
Hanging: 0.25", Space After: 10 pt, Line  
spacing: multiple 1.15 li, No bullets or  
numbering

Neil Lareau 2/11/16 10:56 AM

Deleted:

- 1023 Freitas, S. R., Longo, K. M., Chatfield, R., Latham, D., Silva Dias, M. A. F., Andreae, M.  
 1024 O., and Carvalho Jr, J. A.: Including the sub-grid scale plume rise of vegetation fires  
 1025 in low resolution atmospheric transport models. *Atmos. Chem. Phys.*, 7, 3385-3398,  
 1026 doi:10.5194/acp-7-3385-2007, 2007.
- 1027 Fromm, M., Lindsey, D. T., Servranckx, R., Yue, G., Trickl, T., Sica, R., and Godin-  
 1028 Beekmann, S.: The untold story of pyrocumulonimbus. *Bull. Amer. Meteor. Soc.* 91,  
 1029 1193-1209, DOI:10.1175/2010BAMS3004.1, 2010.
- 1030 Fromm, M., Tupper, A., Rosenfeld, D., Servranckx, R., and McRae, R.: Violent pyro-  
 1031 convective storm devastates Australia's capital and pollutes the stratosphere. *Geophys.*  
 1032 *Res. Lett.*, 33, L05815, doi:10.1029/2005GL025161, 2006.
- 1033 Fromm, M. D., and Servranckx, R. (2003). Transport of forest fire smoke above the  
 1034 tropopause by supercell convection. *Geophys. Res. Lett.*, 30, 1542,  
 1035 doi:10.1029/2002GL016820, 2003.
- 1036 Gatebe, C. K., Varnai, T., Poudyal, R., Ichoku, C., and King, M. D.: Taking the pulse of  
 1037 pyrocumulus clouds. *Atmos. Environ.*, 52, 121-130,  
 1038 doi:10.1016/j.atmosenv.2012.01.045, 2012
- 1039 Jones, T. A., and Christopher, S. A.: Satellite and Radar Observations of the 9 April 2009  
 1040 Texas and Oklahoma Grassfires. *Bull. Amer. Meteor. Soc.*, 91, 455–460. Doi:  
 1041 10.1175/2009BAMS2919.1, 2010.
- 1042 Jones, T. A., and Christopher, S. A.: Satellite and radar remote sensing of southern Plains  
 1043 grass fires: A case study. *Journal of Applied Meteorology and Climatology*, 49, 2133-  
 1044 2146, doi: 10.1175/2010JAMC2472.1, 2010.
- 1045 Kiefer, C. M., Clements, C. B., and Potter, B. E.: Application of a mini unmanned aircraft  
 1046 system for in situ monitoring of fire plume thermodynamic properties. *J. Atmos.*  
 1047 *Oceanic Technol.*, 29, 309-315, doi: http://dx.doi.org/10.1175/JTECH-D-11-00112.,  
 1048 2012
- 1049 Koltunov, A., Ustin, S. L., and Prins, E. M.: On timeliness and accuracy of wildfire  
 1050 detection by the GOES WF-ABBA algorithm over California during the 2006 fire  
 1051 season. *Remote Sens. Environ.*, 127, 194-209, doi:10.1016/j.rse.2012.09.001, 2012.
- 1052 Hogan, R. J., Illingworth, A. J., O'connor, E. J., and Baptista, J. P. V.: Characteristics of  
 1053 mixed-phase clouds. II: A climatology from ground-based lidar. *Quart. J. Roy.*  
 1054 *Meteor. Soc.*, 129, 2117-2134, doi: 10.1256/qj.01.209, 2003.
- 1055 Hogan, R. J., Grant, A. L. M., Illingworth, A. J., Pearson, G. N. and O'Connor, E. J.:  
 1056 Vertical velocity variance and skewness in clear and cloud-topped boundary layers as  
 1057 revealed by Doppler lidar. *Q.J.R. Meteorol. Soc.*, 135: 635–643. doi: 10.1002/qj.413,  
 1058 2009.

1059 Holzworth, G. C.: Estimates of mean maximum mixing depths in the contiguous United  
1060 States, *Mon. Weather Rev.*, 92, 235–242, doi: [10.1175/1520-](https://doi.org/10.1175/1520-0493(1964)092<0235:EOMMMD>2.3.CO;2)  
1061 [0493\(1964\)092<0235:EOMMMD>2.3.CO;2](https://doi.org/10.1175/1520-0493(1964)092<0235:EOMMMD>2.3.CO;2), 1964

1062 Horel, J., Splitt, M., Dunn, L., Pechmann, J., White, B., Ciliberti, C., Lazarus, S.,  
1063 Slemmer, J., Zaff, D., and Burks, J.: Mesowest: cooperative mesonets in the Western  
1064 United States. *Bull. Amer. Meteor. Soc.*, **83**, 211–225.  
1065 doi: [http://dx.doi.org/10.1175/1520-0477\(2002\)083<0211:MCMITW>2.3.CO;2](https://dx.doi.org/10.1175/1520-0477(2002)083<0211:MCMITW>2.3.CO;2),  
1066 [2002](https://doi.org/10.1175/1520-0477(2002)083<0211:MCMITW>2.3.CO;2)

1067 [Lakshmanan, V., Hondl, K., Potvin, C. K., and Preignitz, D.: An improved method for](#)  
1068 [estimating radar echo-top height. \*Wea. and Forecasting\*, 28, 481-488, doi:](#)  
1069 [10.1175/WAF-D-12-00084.1](https://doi.org/10.1175/WAF-D-12-00084.1), 2013.

1070

1071 Lang, T. J., and S. A. Rutledge: Cloud-to-ground lightning downwind of the 2002  
1072 Hayman forest fire in Colorado, *Geophys. Res. Lett.*, 33, L03804,  
1073 doi:[10.1029/2005GL024608](https://doi.org/10.1029/2005GL024608), 2006

1074 Lang, T.J., Steven A. Rutledge, Brenda Dolan, Paul Krehbiel, William Rison, and Daniel  
1075 T. Lindsey: Lightning in Wildfire Smoke Plumes Observed in Colorado during  
1076 Summer 2012. *Mon. Wea. Rev.*, **142**, 489–507. doi: [http://dx.doi.org/10.1175/MWR-](http://dx.doi.org/10.1175/MWR-D-13-00184.1)  
1077 [D-13-00184.1](http://dx.doi.org/10.1175/MWR-D-13-00184.1), 2014

1078 Luderer, G., Trentmann, J., Winterrath, T., Textor, C., Herzog, M., Graf, H. F., and  
1079 Andreae, M. O.: Modeling of biomass smoke injection into the lower stratosphere by  
1080 a large forest fire (Part II): sensitivity studies. *Atmos. Chem. Phys.*, 6, 5261-5277,  
1081 2006, <http://www.atmos-chem-phys.net/6/5261/2006/>.

1082 Luderer, G., J. Trentmann, and M. O. Andreae: A new look at the role of fire-released  
1083 moisture on the dynamics of atmospheric pyro-convection. *Int. J. Wildland Fire*, 18,  
1084 554-562, doi: /10.1071/WF07035, 2009

1085 Markowski P, and Richardson, Y.: *Mesoscale Meteorology in Midlatitudes*. John Wiley  
1086 and Sons, 430 pp, 2011.

1087 McRae, R. H., Sharples, J. J., Wilkes, S. R., and Walker, A.: An Australian pyro-  
1088 tornadogenesis event. *Natural hazards*, 65, 1801-1811, doi: 10.1007/s11069-012-  
1089 0443-7, 2013.

1090 [Melnikov, V. M., Zrnica, D. S., Rabin, R. M., and P. Zhang, P.: Radar polarimetric](#)  
1091 [signatures of fire plumes in Oklahoma, \*Geophys. Res. Lett.\*, 35, L14815,](#)  
1092 [doi:10.1029/2008GL034311](https://doi.org/10.1029/2008GL034311), 2008.

1093 [Melnikov, V. M., Zrnica, D. S., and Rabin, R. M. : Polarimetric radar properties of smoke](#)  
1094 [plumes: A model, \*J. Geophys. Res.\*, 114, D21204, doi:10.1029/2009JD012647](#), 2009.

Neil Lareau 2/11/16 11:05 AM

Formatted: Font:Not Italic

Neil Lareau 2/11/16 11:05 AM

Formatted: Font:Not Italic

Neil Lareau 2/9/16 3:48 PM

Deleted:

Neil Lareau 2/10/16 3:47 PM

Formatted: Font:Not Italic

1096 Muller, B. M., and C.G. Herbster: Fire Whirls: Twisters That Light the Sky.  
 1097 Weatherwise, 67, 12-23, doi: 10.1080/00431672.2014.960326, 2014.

1098 [Pahlow, M., Kleissl, J., Parlange, M. B., Ondov, J. M., and Harrison, D.: Atmospheric](#)  
 1099 [boundary-layer structure observed during a haze event due to forest-fire smoke,](#)  
 1100 [Bound.-Lay. Meteorol., 115, 53–70, doi:10.1007/s10546-004-6350-z, 2005.](#)

1101 Peterson, D. A., Hyer, E. J., Campbell, J. R., Fromm, M. D., Hair, J. W., Butler, C. F.,  
 1102 and Fenn, M. A.: The 2013 Rim Fire: Implications for predicting extreme fire spread,  
 1103 pyroconvection, and smoke emissions. Bull. Amer. Meteor. Soc., 96, 229-247, doi:  
 1104 <http://dx.doi.org/10.1175/BAMS-D-14-00060.1>, 2015.

1105 Potter, B. E.: The role of released moisture in the atmospheric dynamics associated with  
 1106 wildland fires. Int. J. of Wildland Fire, 14, 77-84, doi:10.1071/WF04045, 2005

1107 [Radke, L. F., J. H. Lyons, P. V. Hobbs, D. A. Hegg, D. V. Sandberg, D. E.](#)  
 1108 [Ward: Airborne monitoring and smoke characterization of prescribed fires on forest](#)  
 1109 [lands in western Washington and Oregon, Tech. Rep. PNW-GTR-251, 81For. Serv.,](#)  
 1110 [U.S. Dep. of Agric., Portland, Ore., 1990.](#)

1111 [Radke, L. F., D. A. Hegg, P. V. Hobbs, J. D. Nance, J. H. Lyons, K. K. Laursen, R. E.](#)  
 1112 [Weiss, P. J. Riggan, D. E. Ward: Particulate and trace gas emissions from large](#)  
 1113 [biomass fires in North America, Global Biomass Burning: Atmospheric, Climatic and](#)  
 1114 [Biospheric ImplicationsJ. S. Levine, 209–224, MIT Press, Cambridge, Mass., 1991.](#)

1115 [Reid, J. S., Koppmann, R., Eck, T. F., and Eleuterio, D. P.: A review of biomass burning](#)  
 1116 [emissions part II: intensive physical properties of biomass burning](#)  
 1117 [particles. Atmospheric Chemistry and Physics, 5, 799-825, 2005.](#)

1118 Rosenfeld, D., Fromm, M., Trentmann, J., Luderer, G., Andreae, M. O., and Servranckx,  
 1119 R.: The Chisholm firestorm: observed microstructure, precipitation and lightning  
 1120 activity of a pyro-cumulonimbus, Atmos. Chem. Phys., 7, 645-659, doi:10.5194/acp-  
 1121 7-645-2007, 2007.

1122 [Saleh, R., Robinson, E. S., Tkacik, D. S., Ahern, A. T., Liu, S., Aiken, A. C., and](#)  
 1123 [Donahue, N. M.: Brownness of organics in aerosols from biomass burning linked to](#)  
 1124 [their black carbon content. Nature Geoscience, 7, 647-650. doi:10.1038/ngeo2220,](#)  
 1125 [2014.](#)

1126 Saunders, P. M.: Penetrative convection in stably stratified fluids, Tellus, 14, 177-194,  
 1127 doi: 10.1111/j.2153-3490.1962.tb00130.x, 1962

1128 Scorer, R. S.: Experiments on convection of isolated masses of buoyant fluid. Journal of  
 1129 Fluid Mechanics, 2, 583-594. doi:10.1017/S0022112057000397, 1957.

1130 Trentman, J., Luderer, G., Winterrath, T., Fromm, M. D., Servranckx, R., Textor, C.,  
 1131 Herzog, M., Graf, H.-F., and Andreae, M. O.: Modeling of biomass smoke injection

craig clements 2/13/16 8:07 PM

**Deleted:** Reid, J. S., Koppmann, R., Eck, T. F., and Eleuterio, D. P.: A review of biomass burning emissions part II: intensive physical properties of biomass burning particles, Atmos. Chem. Phys., 5, 799-825, doi:10.5194/acp-5-799-2005, 2005. .

Neil Lareau 2/11/16 10:47 AM

**Formatted:** Font:Not Italic

Neil Lareau 2/11/16 10:47 AM

**Formatted:** Font:Not Italic

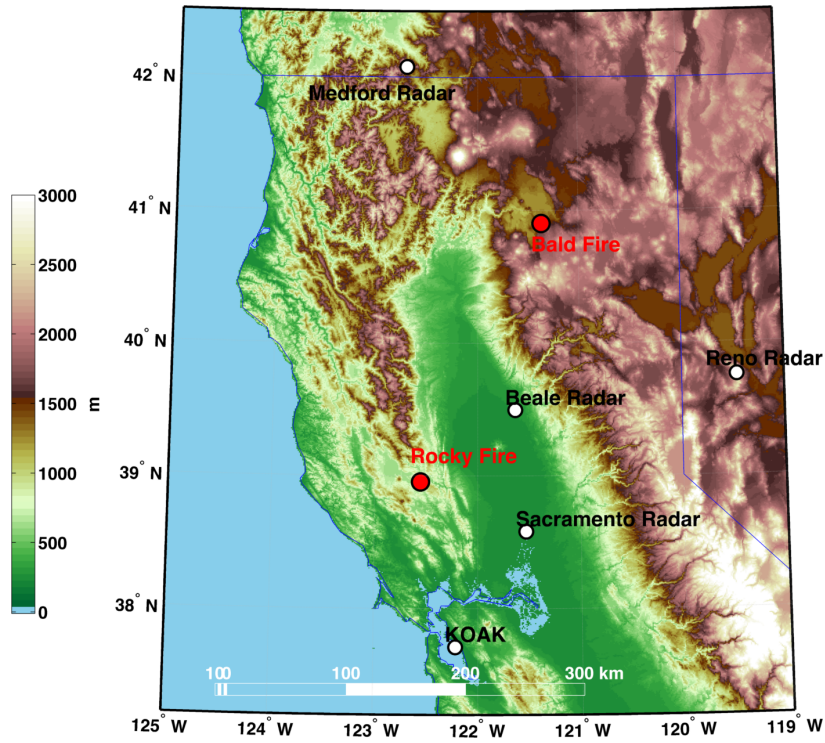
Neil Lareau 2/11/16 10:33 AM

**Formatted:** Font:Not Italic

Neil Lareau 2/11/16 10:33 AM

**Formatted:** Font:Not Italic

- 1138 into the lower stratosphere by a large forest fire (Part I): reference simulation. Atmos.  
1139 Chem. Phys., **6**, 5247–5260, doi: 10.5194/acp-6-5247-2006, 2006.
- 1140 [Winker, D., Vaughan M. A., Omar, A., Hu, Y., Powell, K. A., Liu, Z., Hunt, W. H.,](#)  
1141 [and Young, S. A.: Overview of the CALIPSO mission and CALIOP data processing](#)  
1142 [algorithms, J. Atmos. Oceanic Technol.,\*\*26\*\*, 2310–2323, doi:](#)  
1143 [10.1175/2009JTECHA1281.1, 2009](#)
- 1144 Woodward, B.: The motion in and around isolated thermals. Quarterly Journal of the  
1145 Royal Meteorological Society, **85**, 144-151, doi: 10.1002/qj.49708536619, 1959.
- 1146 Wooster, M. J.: Small-scale experimental testing of fire radiative energy for quantifying  
1147 mass combusted in natural vegetation fires. Geophys. Res. Lett., **29**, 2027,  
1148 doi:10.1029/2002GL015487, 2002
- 1149
- 1150



1151

1152 Fig. 1. Overview map showing the regional topography (terrain shading), locations of the  
 1153 Rocky and Bald Fires (red circles), the locations and names of the NWS radars used in  
 1154 the plume analysis (white circles), and the KOAK sounding site (white circle).

1155

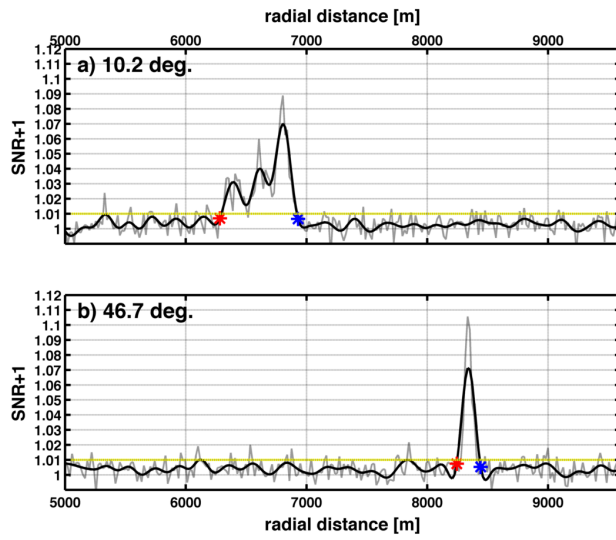
1156

1157

1158

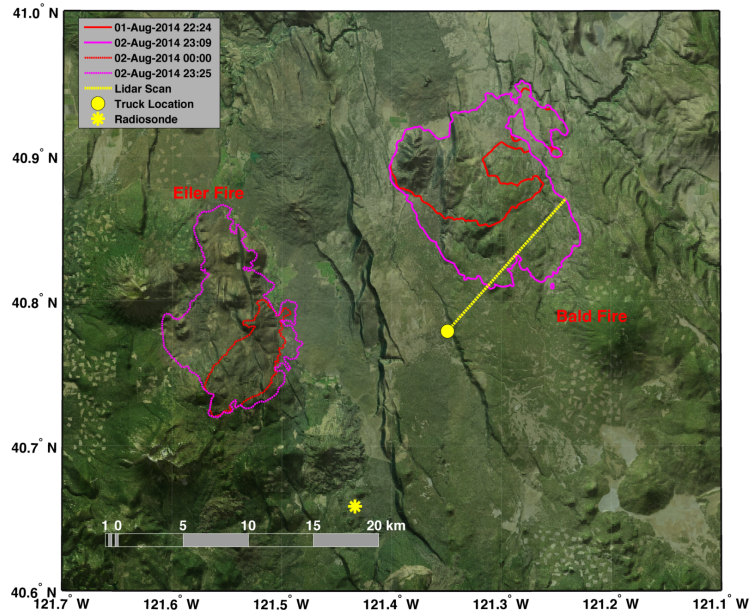
1159

1160



1161

1162 Fig. 2. Examples of the plume detection and attenuation algorithm based on the filtered  
 1163 (solid black line) and unfiltered (gray line) lidar signal-to-noise ratio (SNR+1). (a) Low  
 1164 elevation angle (10.2 deg) lidar beam intersecting the base of the Bald Fire convective  
 1165 column. (b) High elevation angle (46.7 deg) beam intersecting the pyroCu in the upper  
 1166 plume. The red stars indicate the leading plume edge and the blue stars the attenuation  
 1167 point. The SNR+1 threshold of 1.01 is indicated with a dashed yellow line.  
 1168



1169

1170 Fig. 3. Bald and Eiler Fire progression map for 1 and 2 August. The fire perimeters are  
 1171 from the US National Forest Service National Infrared Operations (NIROPS) flights. The  
 1172 background is a satellite image draped over the terrain, which is highlighted with hill  
 1173 shading. Also shown are the truck location (yellow dot), lidar scan path (yellow line), and  
 1174 radiosonde location (yellow star).

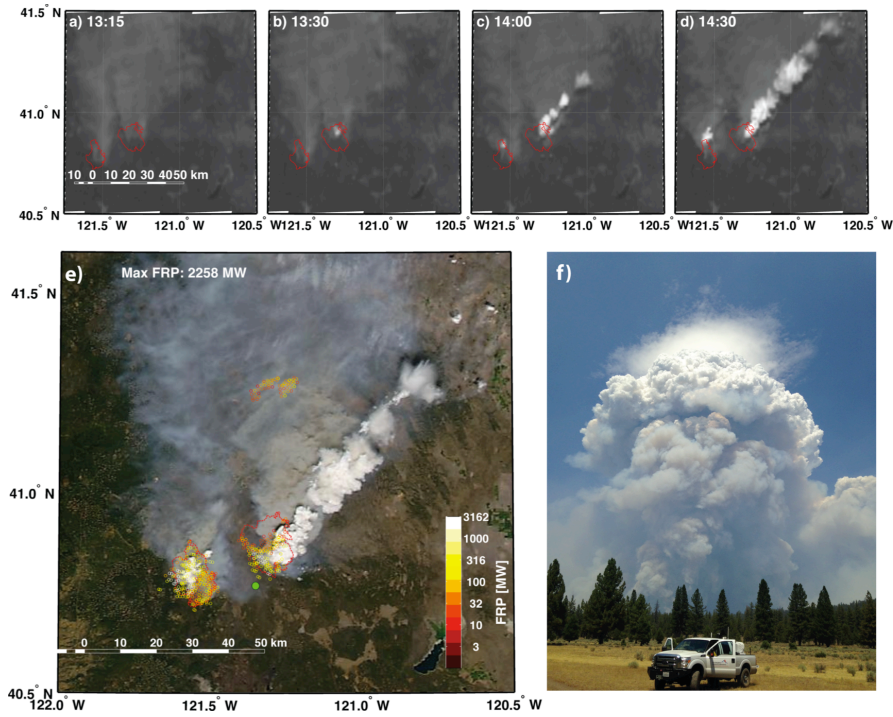


Fig. 4. Overview of the pyrocumulus initiation and growth on 2 August 2014. (a-d) GOES-15 visible imagery showing the pyroCu initiation. (e) MODIS-Aqua visible image at 1426 PDT along with fire-radiative power (FRP, colored circles). (f) Photograph of the lidar vantage point and the windward edge of convective column and pyroCu at 1401 PDT. The truck location is indicated in as a green dot in panel (e). The fire perimeters are as in Fig. 3.

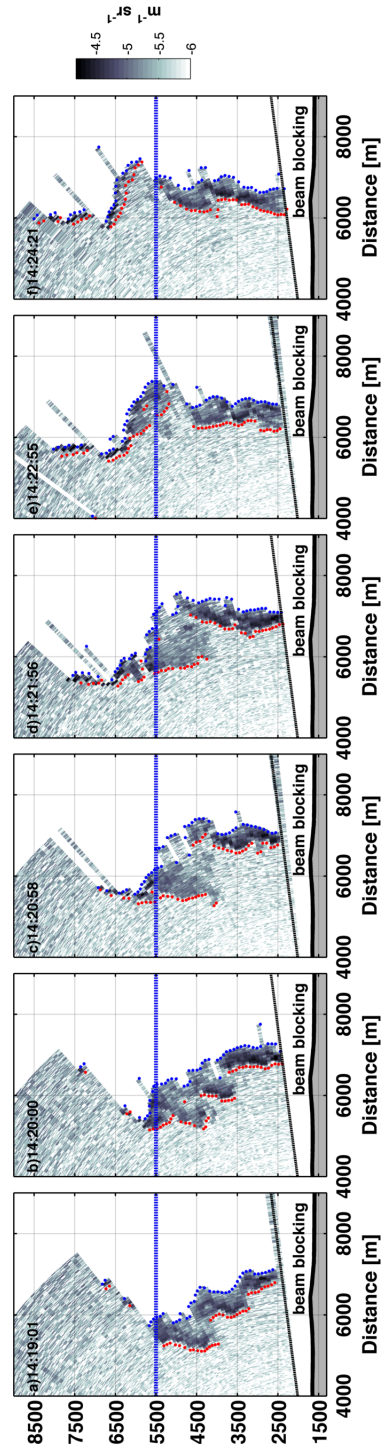


Fig. 5. Plume rise sequence recorded by successive lidar RHI scans from 1419 to 1424 PDT. The displayed data are the logarithmic attenuated backscatter coefficient ( $\text{m}^{-1} \text{sr}^{-1}$ ). The plume edge and attenuation points are shown in red and blue dots, respectively. Data beyond the attenuation point is shadowed (blank points). The dashed blue line indicates the condensation level.

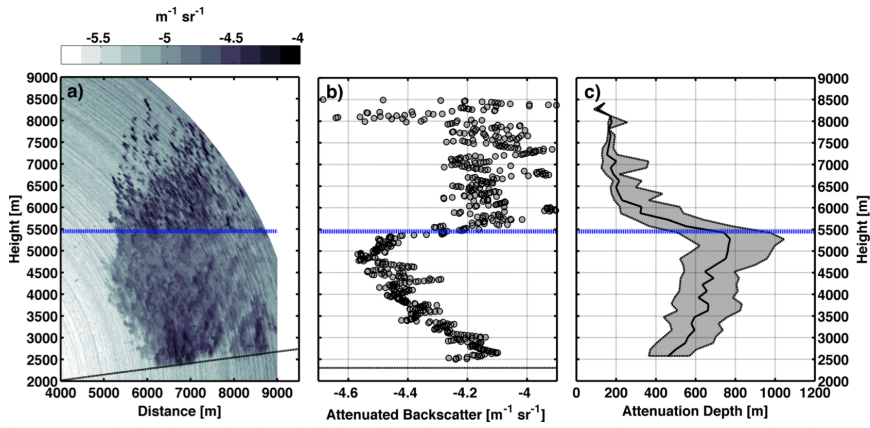


Fig. 6. Statistical analysis of lidar data between 1350 and 1502 PDT showing the plume condensation level. (1) Maximum backscatter as a function of height and distance. (b) Maximum backscatter as a function of height only. (C) 5, 50 and 95<sup>th</sup> percentiles of the attenuation depth as a function of height. The dashed blue line indicates the inferred condensation level.

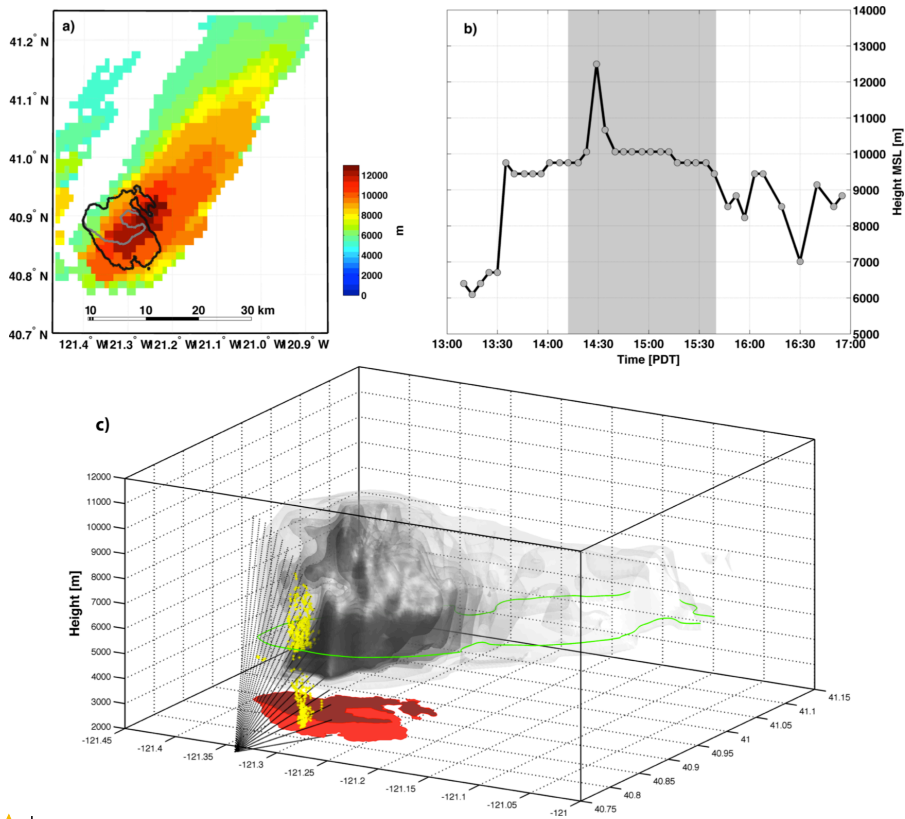


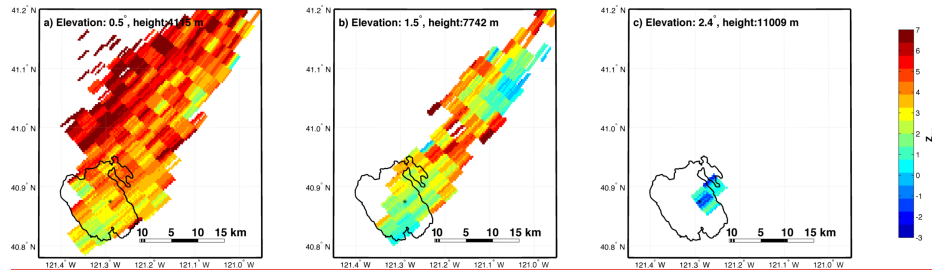
Fig. 7. Radar analysis of the Bald Fire convective column. (a) Maximum echo top heights (color shading) during the Bald Fire along with the NIROPS fire perimeters (gray and black contours). (b) Time series of the maximum echo tops heights. Gray shading shows the period of lidar observations. (c) Volume rendering of the Bald Fire plume at 1429 PDT. Reflectivity isosurfaces are displayed at 30, 28, 26, 24, 22 and 18 dbZ. The lidar scan path and plume detections are shown in black and yellow dots, respectively. Fire perimeters are shown in red shading. The lidar derived condensation level is indicated by the green contour.

Unknown

Formatted: Font:(Default) Times New Roman

Neil Lareau 2/10/16 9:23 AM

Comment [3]: Updated this figure with two new panels showing the time series and 3D rendering



1179  
1180

1181 Fig. 8. Differential reflectivity ( $Z_{dr}$ ) analysis of the Bald Fire plume at 1429 PDT. (a-c)  
1182  $Z_{dr}$  at the 0.5, 1.5, and 2.4 deg. elevation sweeps. The black contour shows the fire  
1183 perimeter on 2 August.

1184

1185  
1186  
1187  
1188  
1189  
1190  
1191  
1192  
1193  
1194  
1195  
1196  
1197  
1198  
1199  
1200  
1201  
1202  
1203  
1204  
1205  
1206

Neil Lareau 2/10/16 9:23 AM  
Comment [4]: This is a new figure

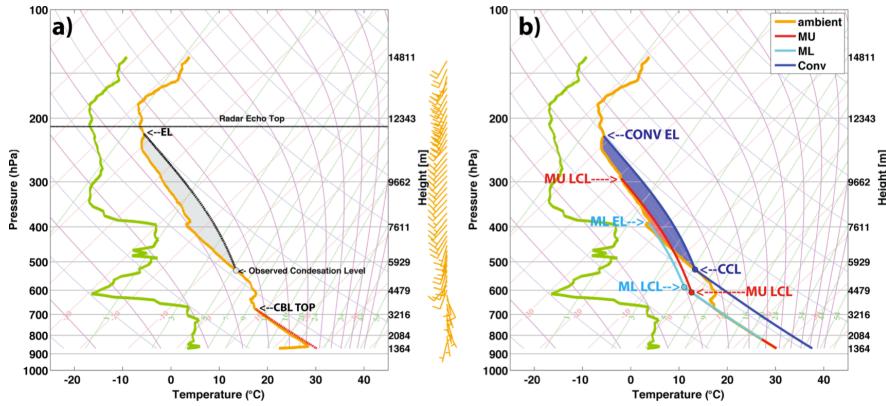


Fig. 9. Thermodynamic analysis of the ambient environment and plume parcels. (a) Observed sounding from [2 August 2014](#), 2100 PDT showing the adjusted boundary layer profile (dashed red line), the lidar derived condensation level (gray circle), the moist-adiabatic ascent from the condensation level, equilibrium level, and the radar derived echo tops. (b) Analysis of lifted parcels, showing the most unstable (MU), mixed-layer (ML), and convective (CONV) parcel trajectories. The condensation and equilibrium levels for each parcel are shown, and their CAPE is shaded.

1208  
1209  
1210  
1211  
1212  
1213  
1214  
1215  
1216  
1217  
1218  
1219  
1220  
1221  
1222  
1223  
1224  
1225  
1226  
1227  
1228  
1229  
1230  
1231  
1232  
1233  
1234  
1235  
1236  
1237  
1238  
1239  
1240  
1241  
1242  
1243  
1244  
1245  
1246  
1247  
1248

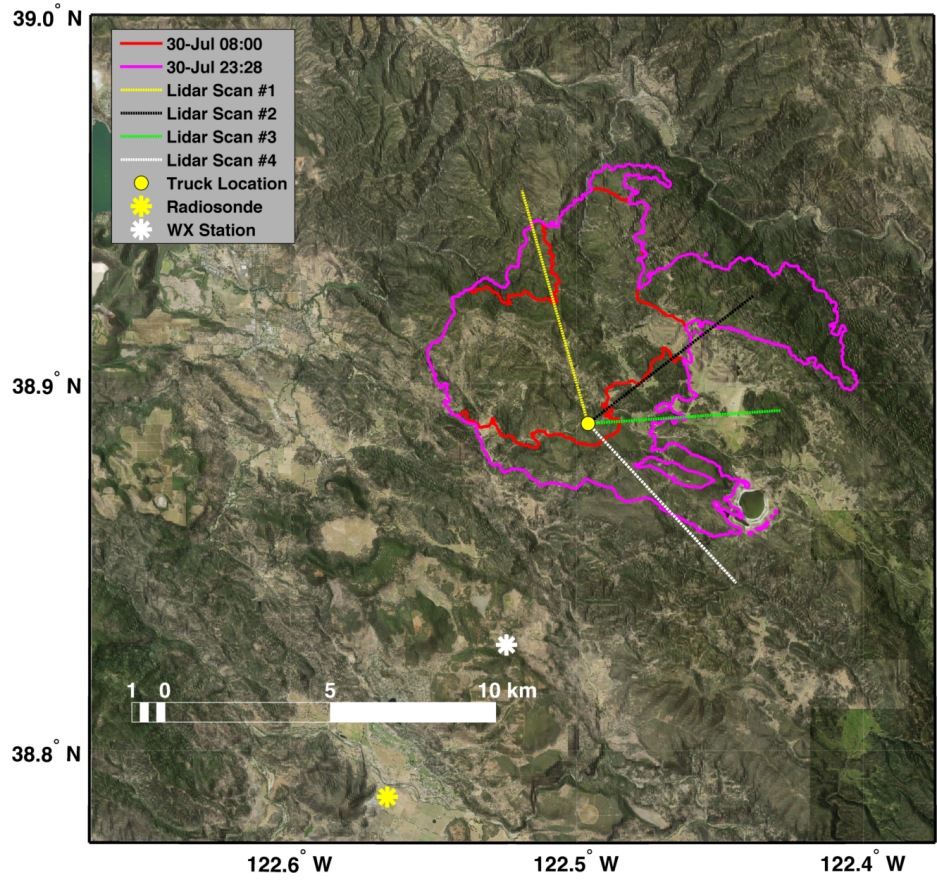


Fig. 10. Rocky Fire progression map for 30 July 2015. The fire perimeters are from the US National Forest Service National Infrared Operations (NIROPS) flights. The background is a satellite image draped over the terrain, which is indicated with hill shading. Also shown are the truck location (yellow dot), lidar scan paths (colored lines), radiosonde location (yellow star), and weather station location (white star).

1249  
1250  
1251  
1252  
1253  
1254  
1255  
1256  
1257  
1258  
1259  
1260  
1261  
1262

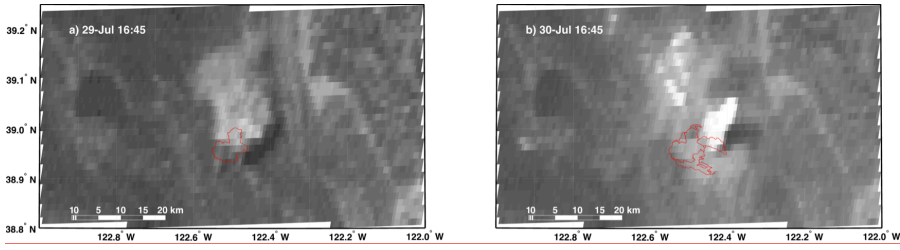


Fig. 11. Visible satellite (GOES-15) images showing the difference in the Rocky Fire plume between 1645 PDT on 29 and 30 July. The data show a pyroCu tower on 30 July that is absent on 29 July.

1263  
1264

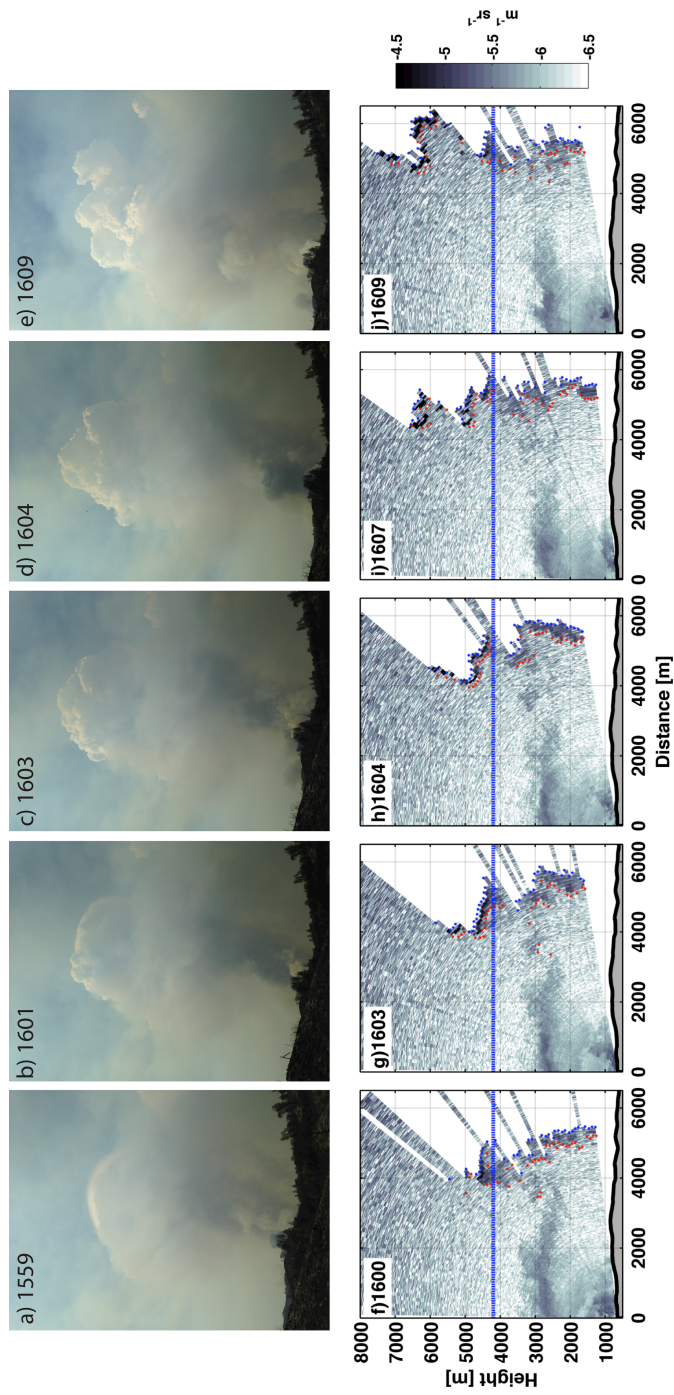


Fig 12. Pyrocumulus development from 1559-1609 PDT on 30 July 2015. (a-e) Photographs of the plume rise and pyroCu development. (f-j) Lidar backscatter showing the onset of condensation and subsequent cloud growth. The dashed blue lines shows the lidar derived condensation level.

1266  
1267  
1268  
1269

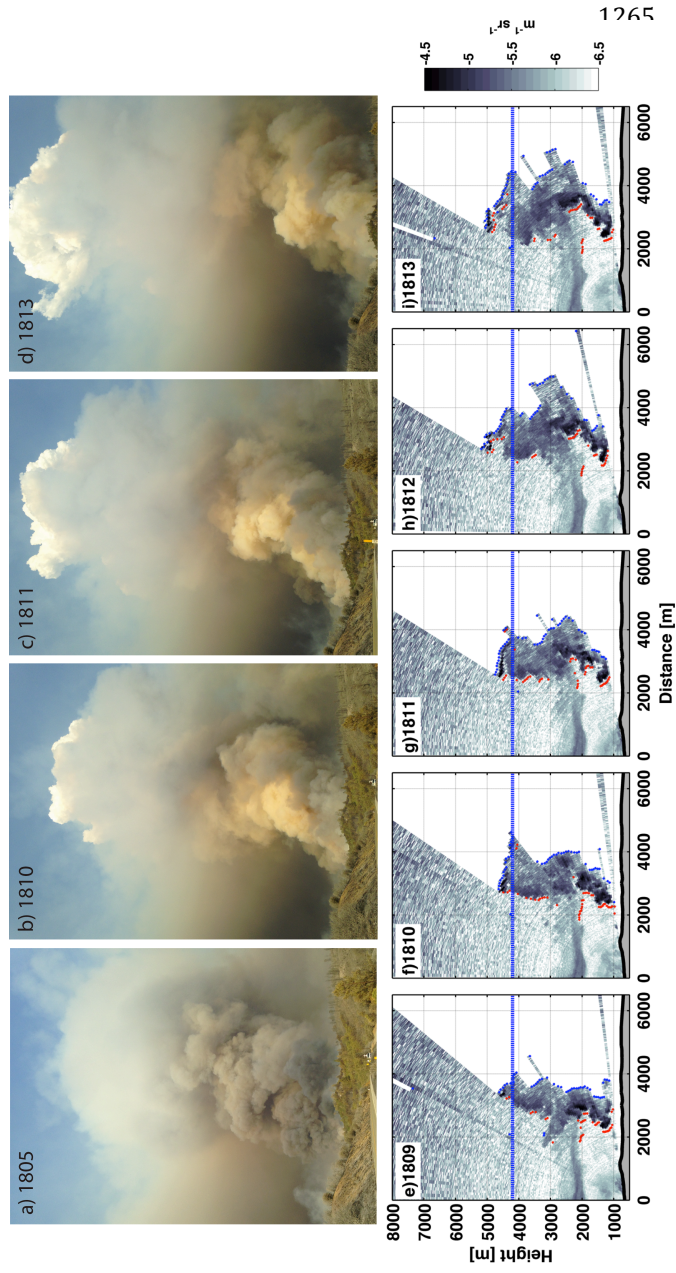
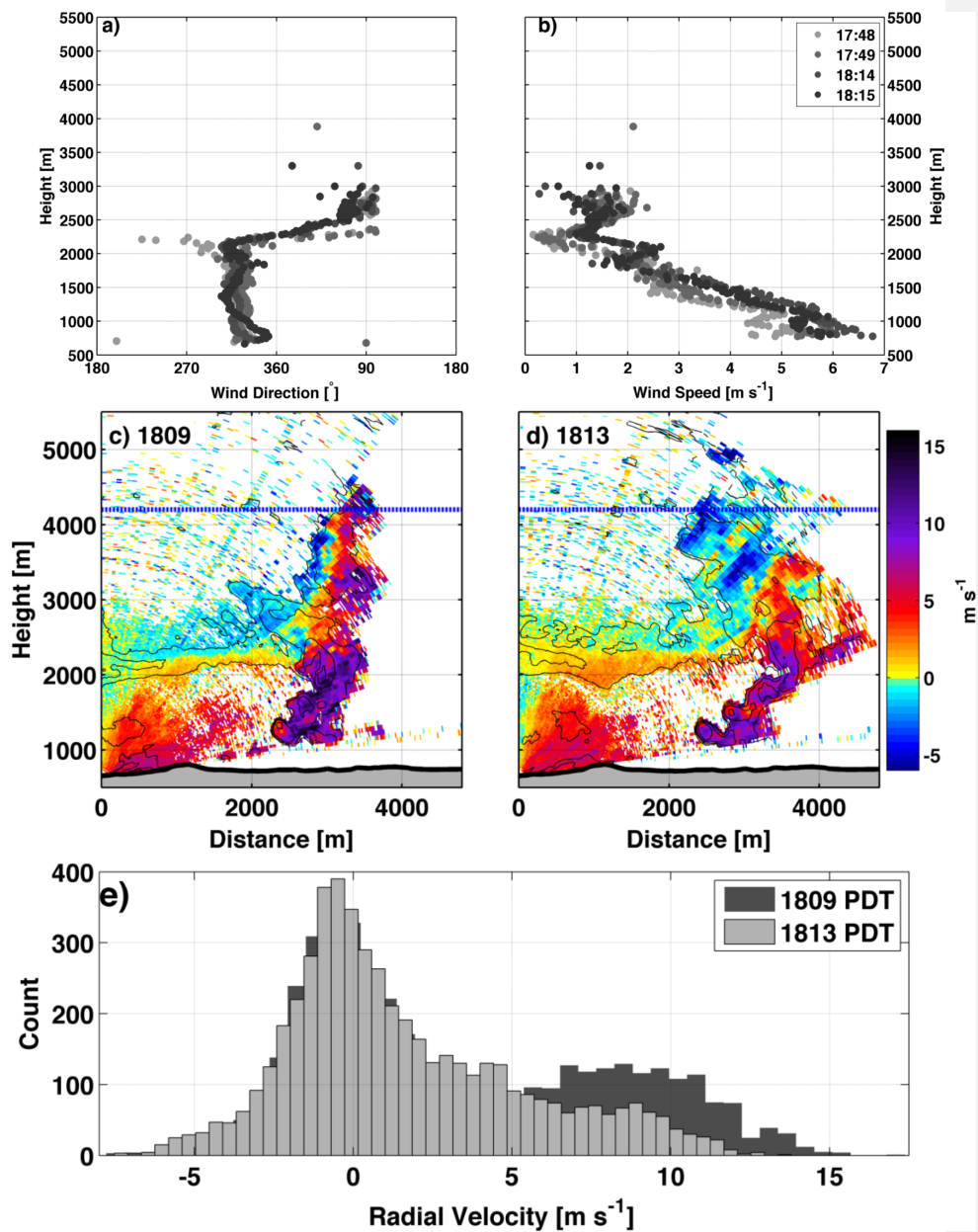
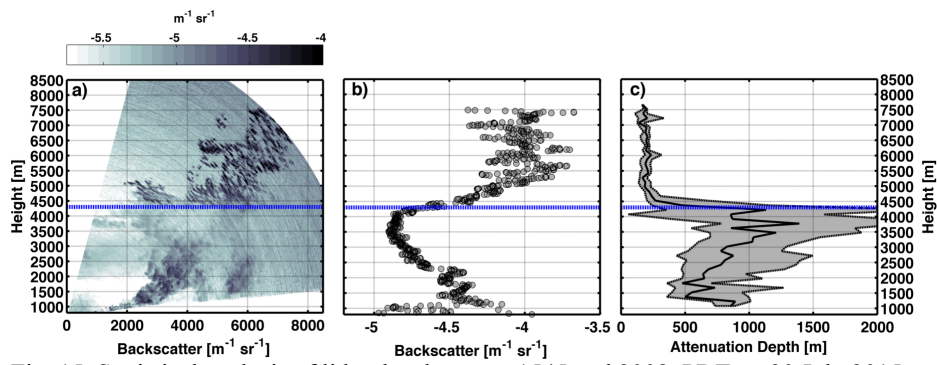


Fig 13. Pyrocumulus development from 1805-1813 PDT on 30 July 2015. (a-d) Photographs of the plume rise and pyroCu development. (e-i) Lidar backscatter showing the onset of condensation and subsequent cloud growth. The dashed blue lines shows the lidar derived condensation level.



1270  
 1271  
 1272  
 1273  
 1274  
 1275

Fig. 14. Analysis of the interaction of the plume with the ambient wind. (a-b) VAD derived profiles of the ambient wind speed and direction. (c-d). Radial velocities during the plume rise and smoke backscatter (black contours). (e) Comparative histogram of radial velocities at 1809 and 1813 PDT.



1276 Fig. 15. Statistical analysis of lidar data between 1545 and 2008 PDT on 30 July 2015.  
 1277 (1) Maximum backscatter as a function of height and distance. (b) Maximum backscatter  
 1278 as a function of height only. (C) Attenuation depth as a function of height. The dashed  
 1279 blue line indicates the inferred condensation level.  
 1280

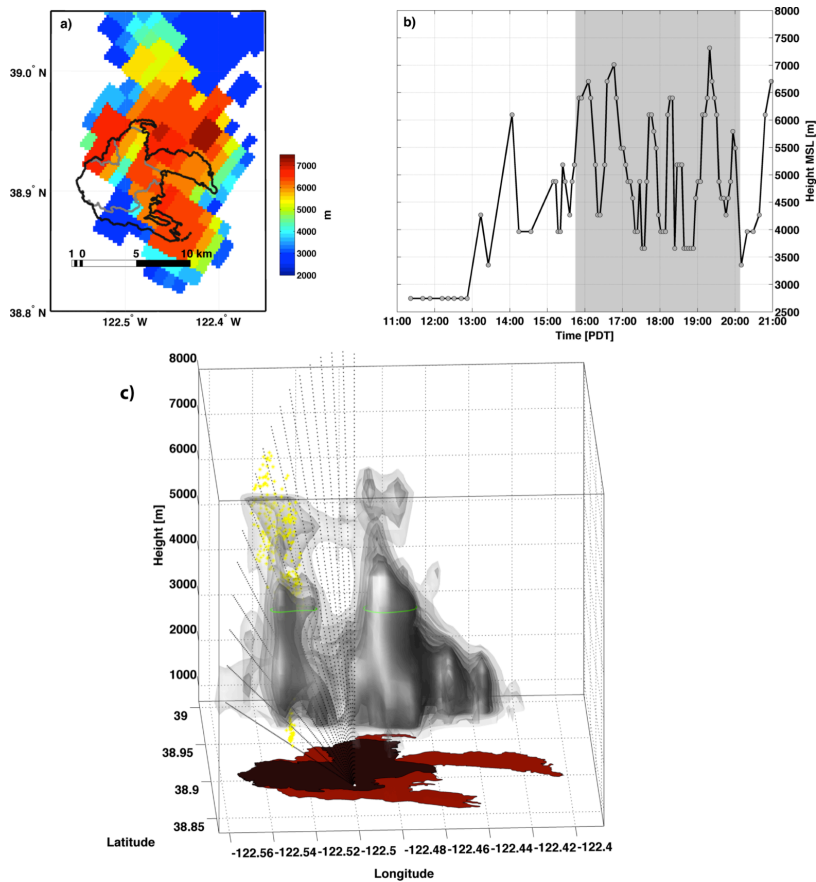


Fig. 16. Radar analysis of the Rocky Fire convective column. (a) Maximum echo top heights (color shading) along with the NIROPS fire perimeters (gray and black contours). (b) Time series of the maximum echo tops heights. Gray shading shows the period of lidar observations. (c) Volume rendering of the Rocky Fire plume at 1609 PDT. Reflectivity isosurfaces are displayed at 30, 28, 26, 24, 22 and 18 dbZ. The lidar scan path and plume detections are shown in black and yellow dots, respectively. Fire perimeters are shown in red shading.

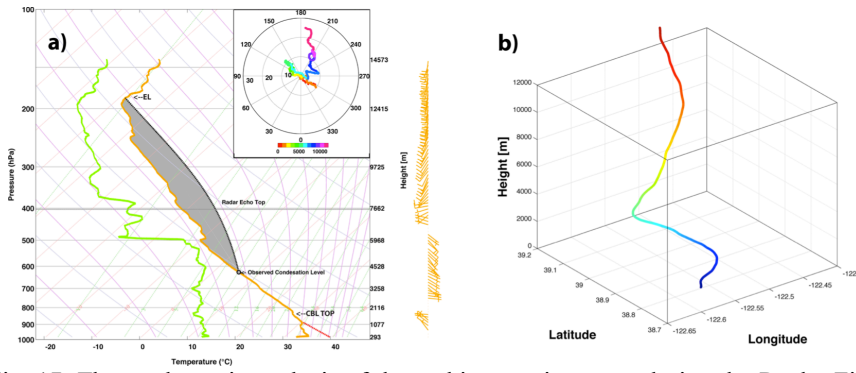
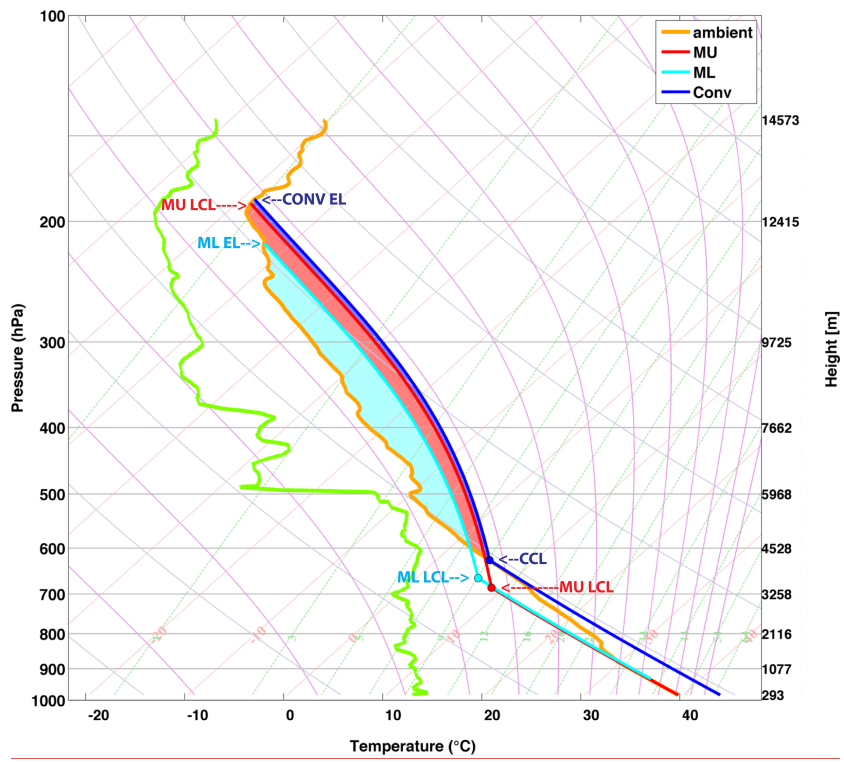


Fig. 17. Thermodynamic analysis of the ambient environment during the Rocky Fire. (a) Observed sounding from 2105 PDT showing the adjusted boundary layer profile (dashed red line), the lidar derived condensation level (gray circle), the moist-adiabatic ascent from the condensation level, and the radar derived echo tops. The inset is a hodograph and the wind barbs on the right indicate how the wind speed and direction change with height. (b) Balloon ascent path showing the affect of wind shear on a buoyant parcel.



1284  
 1285  
 1286  
 1287  
 1288

Fig. 18 Analysis of lifted parcels, showing the most unstable (MU), mixed-layer (ML), and convective (Conv) parcel trajectories. The condensation levels and CAPE for each parcel is described in the text.

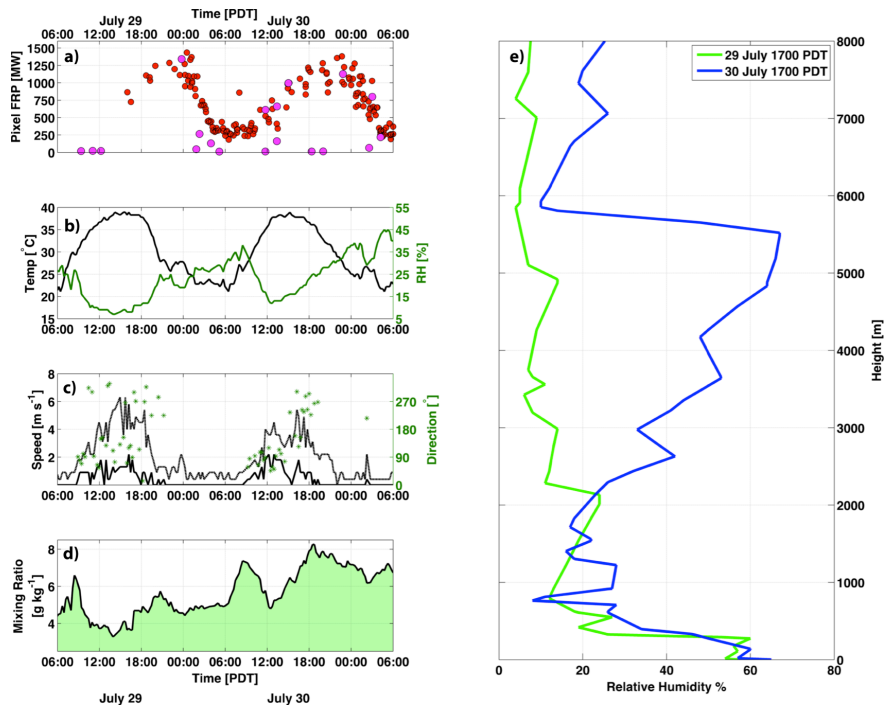


Fig 19. Analysis of the environmental conditions on 29 and 30 July. (a) Fire radiative power from GOES-15 (red dots) and MODIS (purple dots). (b) Temperature (black line) and relative humidity (green line) time series. (c) wind speed (black line), gust (dashed black line) and direction (green stars). (d) Surface mixing ratio. (e) Comparison of the vertical profile of relative humidity from the KOAK sounding at 1700 PDT on 29 and 30 July. The location of the weather station is shown in Fig. 10.